Directional Pair-Correlation Analysis of Fracture Networks

François Bonneau, Dietrich Stoyan

JGR Solid Earth

RESEARCH ARTICLE
10.1029/2022JB024424

Directional Pair-Correlation Analysis of Fracture Networks

François Bonneau[1] and **Dietrich Stoyan**[2]

[1]Université de Lorraine, CNRS, GeoRessources, Nancy, France, [2]Institut für Stochastik, TU Bergakademie Freiberg, Freiberg, Germany

Key Points:

- Variability statistics of fracture networks are based on distances between object barycenters, measured along dominant orientations
- An artificial network based on a simple structure serves as a benchmark; the method is tested on two natural fracture networks
- Important aspects of spatial correlation and variability are visualized and measured via pair-correlation functions

Supporting Information:

Supporting Information may be found in the online version of this article.

Correspondence to:

F. Bonneau,
francois.bonneau.noury@gmail.com

Citation:

Bonneau, F., & Stoyan, D. (2022). Directional pair-correlation analysis of fracture networks. *Journal of Geophysical Research: Solid Earth*, *127*, e2022JB024424. https://doi.org/10.1029/2022JB024424

Received 20 MAR 2022
Accepted 6 AUG 2022

Abstract Fractures result from complex mechanical processes producing irregular, hierarchical, and correlated networks. The statistical analysis of such networks is an important step toward characterizing and modeling fractures. However, established exploratory statistics for the investigation and quantification of fracture networks use only first-order or mean-value characteristics such as the density or the length and orientation distributions of fractures, leaving much to be desired. Here, we present a second-order statistical theory to characterize the inner variability of fracture networks in 2D. We use ideas from marked point process theory treating the barycenters of fractures or fracture branches as "points" and fracture lengths and orientation as "marks." The statistics are based on oriented distances between object centers, which are represented by pair-correlation and mark-correlation functions describing fracture network variability. The forms of the corresponding plots give information on the degree of randomness, the most frequent center-to-center distances, and possible local order, all with respect to fracture orientations. We demonstrate the application of these ideas by analyzing three fracture networks. First, we study a synthetic structure as a benchmark test of the methods under ideal conditions. Then, we focus on two previously characterized field exposures: a well-developed and highly connected network and a very irregular network with many small and isolated fractures. The correlation functions successfully characterize the different spatial arrangements of fractures in all three cases.

Plain Language Summary Fractures have a tremendous impact on the stability, hydraulic properties, and other aspects of rock bodies. Describing and understanding the geometry and organization of fracture networks is therefore both an academic and industrial issue. One way to tackle this problem is to study fracture network geometries in surface exposures. The classical first step in describing the statistics of a fracture network is to determine the number and density of fractures. This paper furthers this approach by presenting methods to describe the variability within fracture networks. The basic idea is to describe each fracture as a point (its barycenter) and two associated features (length and orientation) and use methods for the statistical analysis of marked point patterns. These methods statistically analyze the distances between barycenters, measured along the dominant orientations of the network. The results are presented as plots of correlation functions, yielding information on the degree of randomness and local order. As a demonstration, we apply this method to one synthetic and two natural fracture networks, with the synthetic network serving as a benchmark test. This method successfully characterizes the variability in the two natural networks.

1. Introduction

Fractures are mechanical discontinuities in rocks, visible in surface exposures as fracture traces. They form complicated fracture networks that can be understood as collections of simpler components, each with its own geometry. Because of interactions between fractures during their initiation, growth, and termination (Pollard & Aydin, 1988), fracture networks develop particular spatial organizations that can be statistically measured and described. Such characterization is necessary to predict the impact of fractures on the stability of rock bodies, on ore deposits, on fluid flow, and on reservoir capacity and compartmentalization. Therefore, fracture networks are a topic of intensive research; see for example, Hardebol et al. (2015), Lei et al. (2017), Peacock and Sanderson (2018), Laubach et al. (2019), Sui et al. (2019), and references therein for recent reviews and case studies.

As in many prior studies, we here study fracture traces in surface exposures, which we refer to simply as "fractures" hereafter. These fractured exposures are cross-sections of corresponding three-dimensional fracture networks. Such sections provide valuable information, even in the context of three-dimensional modeling (e.g., Bonneau et al., 2016): when testing the goodness-of-fit of simulated or synthetic fracture networks, comparing planar sections to exposure patterns can pave the way to realistic three-dimensional fracture network modeling.

For this purpose, it is important to characterize a fracture network in 2D using informative parameters and statistical summary functions. Since realistic three-dimensional models will be based on mechanical assumptions, these geometrical statistics ultimately help understand the mechanical processes that form fracture networks.

An important first step in calculating fracture network statistics is the determination of global mean values. For this purpose, a first-order theory has been developed and extensively used since the early 1980s (see e.g., Dershowitz & Einstein, 1988; Dershowitz & Herda, 1992; Gillespie et al., 1993; Zeeb et al., 2013). Here, "first order" means that spatial mean values are determined, such as the average number of fractures per unit area. Although these characteristics are valuable for general or global descriptions, they do not provide any information on the spatial variability and inner spatial correlations of fracture networks. This limitation was already mentioned by Dershowitz and Einstein (1988), who briefly discussed some early papers in the context of "autocorrelation and correlation." Since then, spatial distributions of fractures have been widely investigated. One of the main approaches is to analyze fracture spacing along scan lines using some statistical analysis that may reveal either clustering of fractures or regular spacing (Gillespie et al., 1993; Shakiba et al., 2022). Another well-known approach uses estimators of fractal dimensions to characterize inner correlations in fracture networks (see the review by Bonnet et al. [2001]).

Here, we incorporate ideas from point process statistics to define second-order characteristics and enrich the classical toolbox for fracture network characterization with descriptors of variability and organization. Following the example of Bonnet et al. (2001) and Darcel et al. (2003a, 2003b), we consider fracture networks as samples of "object models" (Pyrcz & Deutsch, 2014), that is, of marked point processes where the "marks" are geometrical objects; in this case, they are straight-line segments that represent fractures or fragments of fractures called "branches." The "points" are the barycenters of these objects, which are characterized in a natural way by two "marks": (a) trace length and (b) trace azimuth.

The marked point process approach uses well-established functional summary characteristics, which we suggest also apply in the context of fractures. Most of these characteristics have names containing the word "correlation"; indeed, they are related to well-known geostatistical correlation functions (Pyrcz & Deutsch, 2014).

Many studies on the statistics of marked point processes assume isotropy. However, most fracture network data are strongly anisotropic, that is, highly dependent on directionality. We thus consider anisotropy to be an essential feature of fracture networks and accordingly use modified direction-dependent correlation functions. We also separately analyze subfamilies of similarly oriented objects.

To demonstrate our methods, we use them to analyze data from one synthetic and two natural fracture networks. The first natural network was mapped from a satellite image of the Oman Mountains; the second is a surface exposure from the Hornelen Basin (Norway). These data were previously studied using first-order methods by Zeeb et al. (2013) and Odling (1997), respectively, and using fractal methods by Darcel et al. (2003a, 2003b).

We apply second-order statistics to both fractures and fracture branches. Analyzing fracture-center systems yields information about the spatial distribution of fractures, whereas analyzing branch barycenters helps to characterize aspects of the interactions between fractures. For both studied natural fracture networks, our approach highlights significant deviations from a purely random organization and reveals repulsion between fractures, the most frequent center-to-center distances, and spatial periodicity.

2. Fundamentals of Fracture Network Characterization

The combined geometrical and statistical investigation of fracture networks is a well-known challenge. Therefore, we use an approach combining field observations and modeling. Rock mechanics and linear elasticity provide a strong understanding of how fractures appear, propagate, and stop in rock masses (Pollard & Aydin, 1988). This basic mechanical knowledge provides guidelines for statistically characterizing fracture networks, and statistical analysis can be used to supplement and calibrate this theoretical framework; see Schwartz and Sibson (1989) and Scott et al. (2022) for examples in the context of fault segmentation.

This section provides a brief overview of useful mathematical models, assumptions, and the fundamentals of spatial exploratory statistics.

2.1. Modeling Fracture Networks

A highly accurate way to describe a fracture network is to explicitly represent fractures as individual objects in the spirit of object models (Pyrcz & Deutsch, 2014). Each fracture is then characterized by its spatial location, that is, a point c_i, and its own irregular geometry, given by the set X_i.

Obtaining statistics for all of X_i is difficult, even if the fractures were fully observable. Therefore, since the observation conditions are usually limited, the characterization uses models with various simplifying assumptions. The most common mathematical idealization of spatial fracture networks is to consider them as systems of two-dimensional flat surfaces, that is, X_i is assumed to comprise planar objects such as disks, ellipses, or rectangles. This means that apertures and any deviations from a flat shape are ignored.

The sets X_i are randomly scattered in space, where "randomly" does not mean "without any rules" or "totally irregularly." In fact, natural networks show various spatial correlations among fractures: for example, younger fractures often terminate at older ones, and volumes in proximity to fractures are often fracture free due to stress reduction in the shadow zone (Kim et al., 2004; Pollard & Aydin, 1988).

A classical model for three-dimensional fracture networks is the Poisson–Baecher disk model. In this object model, the location points c_i are uniformly distributed in space, and the objects X_i are independent disks (Dershowitz & Einstein, 1988). The planar counterpart of the Poisson–Baecher disk model is the so-called "Poisson–Boolean segment process" (Chiu et al., 2013) with randomly distributed segments. Indeed, it can be shown that a planar section through a Poisson–Baecher disk model yields a collection of linear segments whose centers form a planar homogeneous Poisson process (Chiu et al., 2013). See Stoyan (2021) for a detailed discussion of some modern object models for fracture networks (Bonneau et al., 2016; Cherpeau & Caumon, 2015; Cherpeau et al., 2010; Ivanova et al., 2014; Koike et al., 2015).

Here, we consider fracture networks in 2D, which can be understood as resulting from planar sections through a three-dimensional network. In this planar setting, fracture traces are approximated by straight-line objects X_i (hereafter, simply "fractures"). The corresponding location points c_i are the fracture barycenters in the considered plane. The fractures are characterized by two real-valued quantities, called "marks" in the point process context: their length l_i and azimuth a_i. The a_i are the angles describing the fracture orientations ($\in [0°, 180°[$), measured clockwise from north. Thus, each fracture is uniquely described by a marked point $[c_i; (l_i, a_i)]$. In this way, a fracture network is modeled as a random collection of marked points. Such a marking has already been used in mechanics for modeling microcracks (Konietzky et al., 2020). In mathematics, such collections are called "marked point processes." The theory and statistics for marked point processes are described in, for example, Illian et al. (2008) and Baddeley et al. (2016). There are many distributional characteristics of marked point processes, which will be explained as needed.

In the following, we detail the marked point process approach.

2.2. Fractures and Fracture Branches

In this paper, fracture networks are represented by patterns of segments, with each segment representing a fracture or a part of a fracture called a "branch." Branches are defined based on the topological scheme introduced by Barton and Hsieh (1989), Manzocchi (2002), Sanderson and Nixon (2015), and Saevik and Nixon (2017). The original fracture network is equipped with three types of nodes to characterize its topology (Figure 1c):

1. I nodes, the isolated endpoints of fractures;
2. Y nodes, connections between two fractures, with one terminating on the other; and
3. X nodes, points where two fractures cross.

To construct segments that represent fractures, the two endpoints of a fracture can be connected by a straight line, ignoring deviations from a linear form (Figures 1a and 1b). However, this representation is not necessarily unique because it is not always clear where a fracture ends (Figures 1b1 and 1b2). Fracture branches (i.e., curves between nodes) are uniquely represented by segments connecting nodes (Figure 1d). Segments usually differ somewhat from the original feature they represent; this deviation is smaller for branches than for entire fractures.

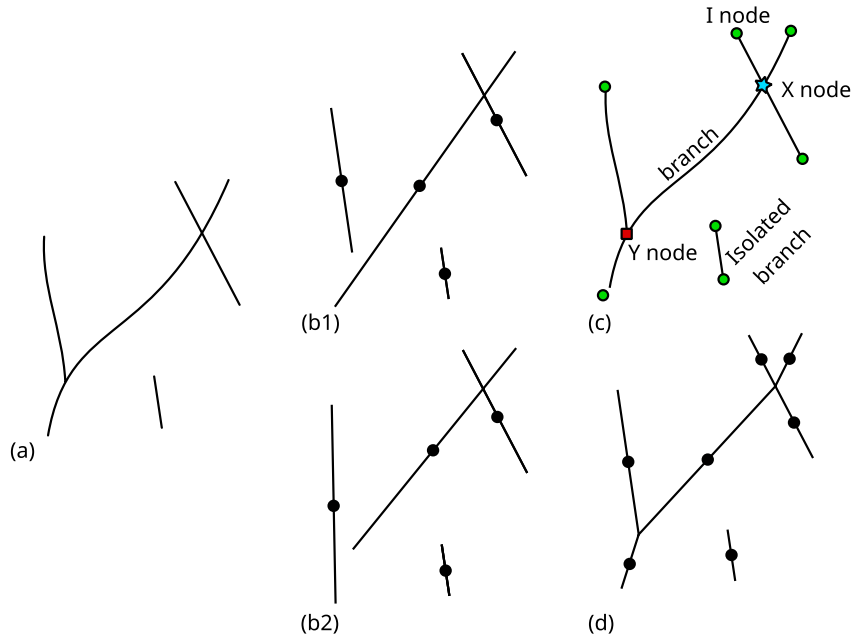

Figure 1. A small fracture network (a) described as a marked point pattern. (b1, b2) Two possible representations of (a), with segments and points representing fractures and their centers, respectively. (c) A topological scheme of the same network, using branches and nodes. (d) The unique representation of (a), with segments and points representing fracture branches and branch centers, respectively.

In the sense of object models, each segment is considered an object. Its barycenter is the point c_i, and its geometrical information is represented by (l_i, a_i) (see Section 2.1). This leads to the classical case of marked point processes with real-valued marks, and standard methods for point process statistics can be applied.

When true fractures are measured in nature, it is possible to measure their full lengths, even if they extend beyond the analytical area (hereafter, "window"), and their corresponding barycenters can be determined (see Manzocchi et al., 2009). However, if the only available information is from within the window, the determination of barycenters becomes nontrivial due to edge effects and/or censoring.

Here, we explain our solution to this problem in the case of an entire fracture. If the fracture is fully contained in the window, c_i is simply the barycenter of the corresponding segment. Otherwise, there are two options according to the relative lengths of the portions of the segment within and beyond the window. If the portion of the segment within the window is shorter than the median of the fracture length distribution, no point is constructed; if longer, c_i is assigned as the barycenter of the portion within the window. If a segment's barycenter is not in the observation window, that is, no point is built, it is included in the first-order characterization but excluded from the second-order characterization.

The question then becomes: which objects should be used to characterize fracture networks, fractures or fracture branches? This decision matters because the patterns of the corresponding barycenters differ greatly in number and distribution. Entire fractures are often very long and their barycenters are therefore very far from large sections of the objects they represent. In contrast, branches are shorter and their barycenters closer to their ends. In the following section, we show that both approaches have their benefits, depending on the nature of the fracture network considered.

2.3. Stationarity

Statistical analyses of spatial data sets often target global conclusions about the entire window of observation. This approach may indeed hold in this context of the global density of fractures. Similarly, the methods discussed in this paper can be used to obtain information about global variability. However, this only makes sense if the chances of observing similar fluctuations are homogeneous throughout the observation window, a property called

"stationarity" in mathematics. In point process statistics, stationarity is an exclusively spatial property, having nothing to do with time. A homogeneous Poisson process is an example of a well-known stationary point process.

A geometrical structure is "stationary" if the statistical distributions of its elements are invariant with respect to spatial translations (leaving the marks unchanged; Chiu et al., 2013). For a marked point process in particular, this implies that (a) the local point density fluctuates everywhere around the same value and (b) marks have similar variabilities everywhere. Then, it is logical to consider a global point density and global mark value distributions.

Although stationarity may be true for theoretical stochastic models, when a real fracture network is investigated, it is fundamental to evaluate if it can be considered a stationary structure. For example, this assumption is not justified if there are clear spatial trends in fracture density or erratic deformations. A good example of statistics in the case of nonstationarity is found in the study of fracture swarms and corridors by Sanderson and Peacock (2019).

When fracture networks are partly affected by local deformation, the stationarity hypothesis may call for restoration to remove any translation and/or rotation due to deformation (Bergbauer & Pollard, 2004; Macé et al., 2004). With this in mind, geologists may be able to isolate subregions where the assumption of stationarity is valid. Bistacchi et al. (2020) give an excellent example of such a regionalization. In contrast, the size of the observation window also has some influence because a small part of a large stationary structure may appear to be a nonstationary pattern. This problem is related to the correct determination of a representative element volume (see e.g., Martinelli et al., 2020, and references therein).

Another geometrical invariance property, isotropy, indicates the invariance of distributions with respect to rotations. This property appears unrealistic in most cases of fracture network statistics, with exceptions of microstructures and fractures created under isotropic horizontal stress (e.g., polygonal fractures, mud-cracks). Nonetheless, we propose to use statistical summary characteristics from the isotropic case and consider them as directional averages.

2.4. Fracture Density Measures

Fracture statistics uses a classical system of numerical measures to quantify the degree of fracturing in rock masses (Dershowitz & Herda, 1992; Dershowitz et al., 2020), which is based on the assumption of stationarity. Different characteristics are represented by "persistence" as P_{ij} (Dershowitz & Einstein, 1988), where i denotes the dimension of the region in which a measurement is taken and j denotes the attribute. Here, we only discuss planar characteristics, namely fracture density P_{20} and fracture intensity P_{21}.

Fracture density is the mean number of fractures per unit area. In object model techniques, where each fracture is represented by a marked point, this is a fundamental point process characteristic called "intensity" (the mean number of points per unit area); here, however, we use geological terms and notation when discussing the number of objects per unit area. For an unbiased statistical estimation of P_{20}, it is recommended to count the number of "bottom" segment endpoints (or southern points on a map) and divide by the window area (Chiu et al., 2013, p. 250; see also Sanderson et al., 2019; Zeeb et al., 2013). The values of P_{20} obtained for the same patterns of fractures considered as networks of entire fractures or of fracture branches are different.

Fracture intensity is the mean of the total fracture trace length per unit area. Various techniques exist for its statistical determination (see Chiu et al., 2013; Zeeb et al., 2013). Based on a mapped surface exposure, image analysis methods can be used to directly determine the total length of all fractures within the observation window, even if they are curved; if the data are sets of linear segments, this determination is even simpler.

2.5. Lengths and Orientations

The lengths l_i of fractures or branches are important quantities. Their values are characterized by the fracture (or branch) "mean length" and "length distribution function." In marked point process theory, such a distribution is a "mark distribution."

The best and simplest method to estimate the mean length of fractures (or branches), without edge effects, is to divide the total length of all segments within the window by the total number of southern endpoints. In contrast, it is difficult to precisely estimate length distributions because of edge effects, which become increasingly important

for smaller window sizes. We recommend and use herein the Miles–Lantuéjoul estimator with minus-sampling (detailed in Appendix A).

Various types of theoretical distributions have been used for fracture (or branch) lengths. Although the power-law distribution is still the most common choice, log-normal, exponential, and gamma distributions are also used (see Bonnet et al., 2001).

Statistically it makes little sense to study the directional mark distribution of the azimuths because short and long fractures/branches would count equally. Therefore, the length-weighted azimuthal distribution collects the directional data into a rose diagram. Rose diagrams help to identify "fracture sets," collections of similarly oriented fractures within the same network, and thus play a central role in this paper.

2.6. Fracture Spacing and Scan Lines

A classical method for studying the spatial organization of fractures is to analyze their spacing along scan lines roughly oriented perpendicular to the strike of fractures. The intersections between these lines and fractures are statistically analyzed using methods for point processes on the real number line.

In this method, the distances between successive points and the corresponding distribution functions and probability densities are analyzed, assuming stationarity (Bistacchi et al., 2020). For a homogeneous one-dimensional Poisson process, the distance distribution is an exponential distribution and the distances are independent (see e.g., Chiu et al., 2013). Knowing that, deviations from this reference case are of special interest. As a measure of comparison, the coefficient of variation Cv is used (Gillespie et al., 1993, 1999), defined as the standard deviation of the spacing distribution divided by its mean. Then, $Cv = 1$ indicates an exponential distribution, whereas $Cv < 1$ indicates a tendency toward regularity and $Cv > 1$ an irregular distribution such as clustering.

Shakiba et al. (2022) introduced second-order statistics for fracture spacings: the one-dimensional analog of Ripley's K-function (see Section 3.1). This method describes clustering and regularity better than by simple comparison with the Poisson process.

Whereas the described methods work under the stationarity assumption, Sanderson and Peacock (2019) analyzed fracture spacings in case of nonstationarity to characterize fracture swarms and corridors.

2.7. Connectivity

Connectivity is an important characteristic of fracture networks because of its impact on the physical behavior of the fractured rock(s). Although a complete review of connectivity measurements is beyond the scope of this paper, we refer the reader to Manzocchi (2002), Renard and Allard (2013), Sanderson and Nixon (2018), and references therein for an overview of connectivity metrics. The number of intersections per fracture C_f has been widely used, particularly in the context of percolation theory (Balberg & Binenbaum, 1983; Berkowitz, 1995; Manzocchi, 2002).

More generally, most connectivity metrics can be defined within the framework of graph theory, the idea being to quantify and characterize intersections of fractures. The topological scheme presented in Section 2.2 is consistent with graph theory; the nodes of the graph are fracture intersections and endpoints (I, Y, and X nodes) and graph edges are fracture branches. This representation has been used to classify fracture networks based on the relative proportions of I, Y, and X nodes (Manzocchi, 2002; Sanderson & Nixon, 2018; Sanderson et al., 2019).

In the present paper, we use both the average number of intersections per fracture C_f and the proportions of I, Y, and X nodes.

3. Second-Order Characteristics for Fracture Networks

Second-order characteristics describe the variability of random structures; "variance" and "correlation" are standard terms in this context. Indeed, the variability of a point pattern can be described by the variance of the number of points present within a test circle placed randomly on the pattern. However, the obtained variance would depend on the shape and size of the test area. Therefore, the statistical theory of point processes uses another approach employing various correlation functions. These functions can be used to calculate, by integration, the

variances of random variables (e.g., the number of points or the sum of marks) in a test area defined by its size and shape (Chiu et al., 2013; Illian et al., 2008).

However, in spatial statistics the main application of these functions is to directly characterize certain aspects of spatial variability. The corresponding statistical estimators consider point pairs, their interpoint distances, and their marks. These distances are then statistically analyzed.

In the present paper, marked point processes are explicitly considered stationary but anisotropic. Nevertheless, we only assume isotropy to simplify the introduction and explanation of the statistical estimators. Furthermore, the corresponding isotropic characteristics are useful as directional averages.

In the following subsections, we introduce various second-order characteristics of marked point processes. We start with characteristics that describe only the points, that is, ignoring their marks: these are Ripley's K-function $K(r)$ and the pair-correlation function $g(r)$, the first being a function of the radius r of a test circle placed randomly within the point process, the second being a function of the distance r between two randomly chosen points. The points' marks are then integrated via mark-correlation functions and anisotropic pair-correlation functions $g(r, \theta)$. The latter employ what are essentially segment orientations θ and are the most important tools presented herein.

Appendix B gives information on the practical estimation of second-order characteristics. The best way is to use R with the SpatStat package.

3.1. Ripley's K-Function

Considering a circle of radius r centered on a randomly selected point in the point process, we count the number of points within the circle, not counting the circle's center. Ripley's K-function describes the expected number of points counted. This number is random, depends on r, and its mean is denoted $S(r) = P_{20}K(r)$. If the point density P_{20} is known, we can define $K(r)$.

Clearly, $K(r)$ is an increasing function of r. Its form gives valuable information on the nature of the point distribution. However, since its definition is based on circles, it is a characteristic of an isotropic point process.

For many point process models, the form of $K(r)$ is theoretically known. Here, we mention only the simplest case, the homogeneous Poisson point process. For this model of complete spatial randomness, it holds simply:

$$K(r) = \pi r^2 \text{ for all } r \geq 0. \tag{1}$$

Ripley's $K(r)$ has values larger than πr^2 for clustered processes, but smaller values for regular processes.

The statistical estimation of $K(r)$ follows its definition. Here, we describe a naive estimator without edge-correction (thus with some bias). Assuming n points c_i in a window W of area $A(W)$, $S(r)$ can be estimated as

$$\hat{S}(r) = \frac{1}{n}\sum_{i=1}^{n} N_i(r), \tag{2}$$

where $N_i(r)$ is the number of points within a circle of radius r and centered at c_i (not counting the circle's center c_i). An estimate of $K(r)$ is then obtained by dividing $\hat{S}(r)$ by an estimate of P_{20}, namely $n/A(W)$. Better estimators of $K(r)$ are described in the literature on point process statistics (e.g., Baddeley et al., 2016; Illian et al., 2008) and are implemented in the SpatStat package of the R software.

The sum in $\hat{S}(r)$ is the same as $n_p(r)$, the number of point pairs within W whose interpoint distances are smaller than r (as used in fractal statistics; Hentschel & Procaccia, 1983). Then:

$$\hat{S}(r) = n_p(r)/n. \tag{3}$$

Thus $K(r)$ is closely related to the "two-point pair-correlation function" $C_2(r)$ (Bonnet et al., 2001):

$$C_2(r) = \frac{2n_p(r)}{n(n-1)}. \tag{4}$$

$C_2(r)$ is used to determine the fractal dimension for fractal point systems: if it scales with r as r^D, the exponent D is called the "correlation dimension." For dimensional estimations, Agterberg (2014) recommends the use of either edge-corrected estimators of point process statistics or the pair-correlation function described below.

A weak point of the K-function is its cumulative nature. The value of $K(r)$ is based on all points in the circle of radius r, independently of their positions within. So it can happen that $K(r)$ has a large value resulting from many points in a close neighborhood of the reference point, while the number of points at with r is small. This makes the interpretation of K-functions difficult. A characteristic free of this disadvantage and showing what happens directly at r is the pair-correlation function.

3.2. Pair-Correlation Functions

Pair-correlation functions ("pcfs") are the main statistical tools applied herein. We first introduce the isotropic pcf, which ignores marks and assumes an isotropic point pattern.

The isotropic pcf $g(r)$ is formally defined as the derivative with respect to r of the K-function, divided by the circumference $2\pi r$:

$$g(r) = \frac{K'(r)}{2\pi r}. \tag{5}$$

Thus, the relationship between $K(r)$ and $g(r)$ is similar to that between a cumulative distribution function $F(x)$ and its corresponding probability density function $f(x)$. The derivative removes the cumulative behavior and the division removes the effect of area growth with increasing r.

A heuristic explanation of $g(r)$, which may aid in its interpretation, is as follows. Consider two deterministic points x and y separated by a distance r. These points are the respective centers of the infinitesimally small circles $b(x)$ of area $\mathrm{d}x$ and $b(y)$ of area $\mathrm{d}y$. The probabilities that a point lies within $b(x)$ or $b(y)$ are $P_{20}\cdot\mathrm{d}x$ and $P_{20}\cdot\mathrm{d}y$, respectively. Under the assumption of isotropy, the probability that there is a point that lies within both $b(x)$ and $b(y)$ depends only on r:

$$p(r) = g(r) \cdot P_{20}\mathrm{d}x \cdot P_{20}\mathrm{d}y, \tag{6}$$

where the isotropic pcf $g(r)$ contains the dependency on r.

In the case of a homogeneous Poisson process, the multiplication theorem of probability theory yields $p(r) = P_{20}\mathrm{d}x\cdot P_{20}\mathrm{d}y$ and $g(r) \equiv 1$ due to the independence properties of the process.

For all reasonable isotropic point processes, the function $g(r)$ takes the value 1 for large r. In fact, for sufficiently large r, the events "there is a point in $b(x)$" and "there is a point in $b(y)$" become independent. Maxima and minima of $g(r)$ mark characteristic values of r that are related to typical interpoint distances. Values of $g(r)$ larger than 1 for small r indicate clustering, whereas values smaller than 1 occur in the case of regularity.

In the case of strong clustering, a pcf can have very large values for small r, and $g(0) = \infty$ is even possible for some point process models. In this case, one speaks of a pole at $r = 0$. If it is known that the point pattern can be considered fractal, and if $g(r)$ scales with r^{-H} for small r (H being a real value), then its fractal dimension D is $D = 2 - H$. However, nonfractal point processes may also have pcfs with a pole at $r = 0$. Therefore, the existence of a pcf pole is not a proof of fractality (Stoyan, 1994).

To estimate $g(r)$ there exists established software (Baddeley et al., 2016; based on the fundamentals explained in Illian et al., 2008). The main idea is to count the number of point pairs at a given interpoint distance r. The interpretation of empirical pcfs is not simple, but we will provide sufficient explanation; we refer interested readers to Illian et al. (2008) for a more thorough explanation.

In the form presented here, $g(r)$ is characteristic of the isotropic case. In the case of anisotropic patterns, we refer to the "isotropic pcf," which is understood as an average over all directions and serves to characterize global interpoint distances. However, to include orientations, we work with the anisotropic pcf $g(r, \theta)$, introduced by Stoyan and Stoyan (1994, p. 286) and explained in Appendix B. It is statistically estimated by counting the number of point pairs of a given interpoint distance r and connected by a line of azimuth approximately equal to θ.

3.3. Mark-Correlation Functions and Variograms

The mark-correlation function $k_{mm}(r)$ characterizes aspects of spatial correlation for a real-valued mark. Here, "mark" is "segment length" and "r" is, as above, the distance between points. As above for $g(r)$, we explain $k_{mm}(r)$ in the isotropic case.

The term $k_{mm}(r)$ is the mean of the products of the marks held by randomly chosen pairs of points separated by a distance r. The corresponding estimator considers every pair of points separated by approximately r and multiplies their marks. The mean of these products is divided by a pair-correlation estimator and by the square of the mean mark, in our case of the mean length. Therefore, $k_{mm}(r)$ has the nature of a conditional mean. A more precise definition is available in Illian et al. (2008).

Because empirical values of $k_{mm}(r)$ are obtained by ratio estimators, for which undesired fluctuations of the numerator and denominator are canceled out, it is acceptable to use mark-correlation functions also when analyzing anisotropic patterns Illian et al. (2008, p. 355).

If the marks are independent, $k_{mm}(r)$ has a theoretical value of 1 for all r. For small r, $k_{mm}(r) < 1$ indicates that nearby segments tend to be shorter than the mean segment length of the fracture network. For large r, as mark values become independent, $k_{mm}(r)$ tends toward the theoretical value of 1.

The mark-variogram $\gamma_m(r)$ is a function similar in nature to $k_{mm}(r)$, but instead of the products of marks, the half-squared differences are used (like in the classical semivariogram) and the function is not normalized. The mark-variogram can also be used in anisotropic cases because it does not depend on the absolute values of marks, only their relative differences.

For large r, the theoretical value of a mark-variogram is equal to the variance σ_m^2 of the marks. For small r, $\gamma_m(r) < \sigma_m^2$ indicates that the marks of nearby points tend to be similar.

The statistics of mark-correlation functions are detailed in Illian et al. (2008).

4. Analysis of an Artificial Fracture Network

In this section, we study the Poisson–Boolean segment process (Section 2.1) as a very simple stochastic model in which the segments represent fractures. This analysis under ideal conditions will serve as a benchmark and help to understand the first- and second-order characteristics of a fracture network with a high degree of randomness.

We consider a special Poisson–Boolean segment process, with fracture density $P_{20} = 0.2\ \mathrm{m}^{-2}$, where all segments are 5 m long and oriented randomly in one of three directions (0°, 90°, and 130°) with equal frequency. In its simulation, the fracture barycenters are distributed in a 105 m × 105 m window as uniform random points at density $P_{20} = 0.2\ \mathrm{m}^{-2}$. Although this example uses a 100 m × 100 m observation window W, we begin with the larger window size to avoid edge effects; segments whose centers lie outside of W can still contribute to the fracture distribution. Segments representing fracture branches are then built from the same pattern, considering the intersections of fractures.

Figure 2 shows a typical realization of this model. The fractures are highly connected and produce many branches. In this example, only 9.0% of the segments represent isolated fractures. The three subsets of fractures or branches with similar orientations are referred to as N0, N90, and N130.

4.1. First-Order Characteristics

Here, we apply the methods described in Section 2 to statistically analyze the simulated pattern.

Although the empirical fracture density P_{20} is near the theoretical value of $0.2\ \mathrm{m}^{-2}$ (with a small statistical deviation), that of the branches is much larger at $0.75\ \mathrm{m}^{-2}$.

Concerning the marks, because the fractures are exact linear segments, the rose diagrams of fracture and branch orientations are identical, following the three chosen directions. In contrast, the distributions of fracture and branch lengths differ (Figure 3). Although the fractures have a constant length of 5 m, branch lengths are variable and have a strongly asymmetric distribution, with the median length ($M_1 = 1.01$ m) significantly smaller than

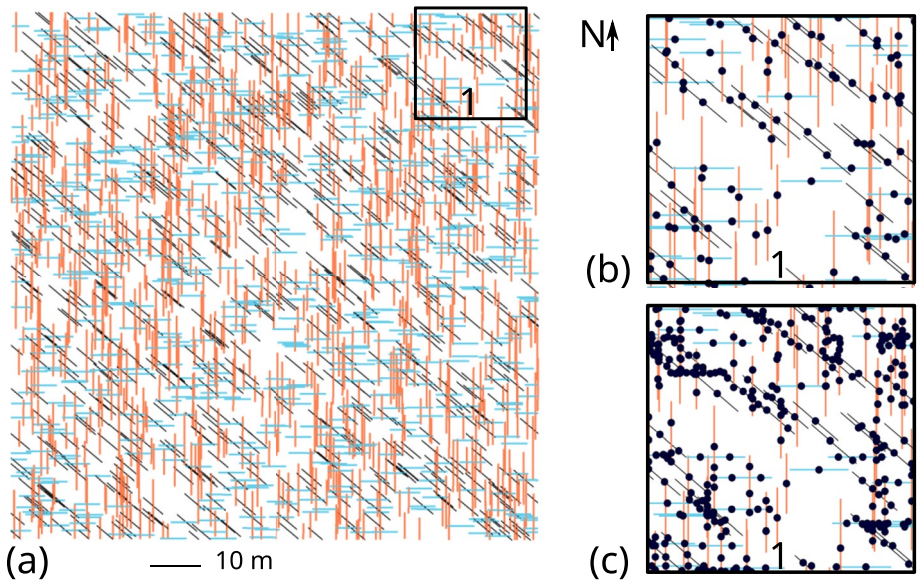

Figure 2. (a) 2D map of an artificial fracture network comprising three fracture sets oriented 0° (red), 90° (blue), and 130° (black). The black square (1) indicates the area shown in (b) and (c). (b) Fracture centers: points of a homogeneous Poisson process. (c) Branch centers constructed by the median rule: a clustered point pattern.

the mean (m_l = 1.36 m). Following the recommendations discussed in Section 2.5 and Appendix A, objects not completely within the observation window are not used to estimate the length distribution. Of course, these objects contribute to the estimation P_{21} and P_{20}.

The empirical first-order characteristics for fractures and branches of the three subsets N0, N90, and N130 are presented in Table 1. Consistent with the findings of Manzocchi (2002), the probability of occurrence of Y nodes in such a stochastic model is very low: indeed, no Y nodes were created in this simulated artificial fracture network.

4.2. Second-Order Characteristics

Here, we focus on the spatial organization of fracture and branch centers. In this example, we have the advantage that the exact fracture centers are known. For validation, we performed the second-order analysis to estimate both the isotropic and anisotropic pcfs, taking care to account for censoring (Section 2.2) and check true versus estimated fracture centers. We observed no significant differences in the results and report here those obtained using estimated fracture centers. In fact, no points were created for fractures partly inside the window because their lengths were shorter than the median (5 m).

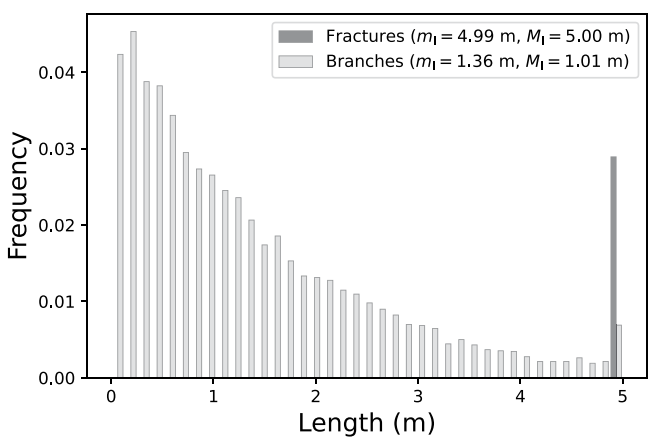

Figure 3. Length distributions of fractures and branches in the artificial fracture network shown in Figure 2.

4.2.1. Pair-Correlation Functions: All Fractures

Figure 4 shows empirical isotropic and anisotropic pcfs for the entire pattern of fractures and branches. The directions θ considered for the anisotropic pcfs $g(r, \theta)$ are the fracture strike azimuths of the sets N0, N90, and N130.

The curves for fracture centers have a very simple form (constant values with small statistical fluctuations around the theoretical value of 1; Figure 4a) because they belong to homogeneous Poisson processes.

In contrast, the pcfs for branch centers have a quite different form. They have very large values for small r and tend to 1 for large r. This form is typical of so-called "cluster point processes." It even seems to make sense to assume that poles to the pcfs exist at $r = 0$. This indicates some form of heavy clustering, which can be explained by the spatial arrangement of branches:

Table 1
First-Order Characteristics of the Artificial Fracture Network

	Fractures				Fracture branches			
	Full set	N0	N90	N130	Full set	N0	N90	N130
P_{20} (m^{-2})	0.200	0.0667	0.0656	0.0673	0.730	0.263	0.244	0.223
P_{21} (m^{-1})	1.02	0.340	0.340	0.340	1.02	0.340	0.340	0.340
m_l (m)	4.99	4.94	5.02	5.01	1.36	1.27	1.35	1.48
M_l (m)	5.0	5.0	5.0	5.0	1.01	0.96	0.98	1.12
Connectivity								
C_f	2.66	2.94	2.73	2.31				
$p_{I\ nodes}$	0.60	0.58	0.59	0.63				
$p_{Y\ nodes}$	0	0	0	0				
$p_{X\ nodes}$	0.40	0.42	0.41	0.37				

Note. M_l and m_l are the median and mean lengths, respectively.

because they result from fracture intersections, branch centers are aligned on fractures and branches have stochastic lengths. Consequently, many branch centers form subpatterns similar to pieces of a linear Poisson processes. In a point process model where the points were randomly scattered along randomly scattered segments, the pcf wrongly suggests a fractal behavior (Stoyan, 1994); in this case, the existence of a pole of the pcf at $r = 0$ was proved mathematically. We assume that a similar situation applies in our case. Furthermore, this effect is increased here because each intersection is associated with four branch sequences (X nodes).

The pcf values nearing 1 at $r > 5$ m are a consequence of the constant fracture lengths: indeed, at distances larger than 5 m, point pairs belong to different fractures and are no longer spatially correlated.

4.2.2. Pair-Correlation Functions: Subset N0

Now, we focus on subset N0, that is, all objects striking 0° (red in Figure 2). The empirical isotropic and anisotropic pcfs of these objects and those perpendicular to them ($\theta = 90°$) are shown in Figure 5.

We observe a similar behavior to that for the entire set, which is also the case for the subsets N90 and N130. For fractures, the centers of the N0 subset again belong to a homogeneous Poisson process, as do those of the N90 and N130 subsets. For branches, the large values of $g(r, 0°)$ at small r again result from sequences of points aligned on fractures. Orthogonally, at $\theta = 90°$, $g(r, 90°)$ has smaller values than $g(r, 0°)$ for small r, indicating that features oriented at $\theta = 0°$ are not aligned in the orthogonal direction.

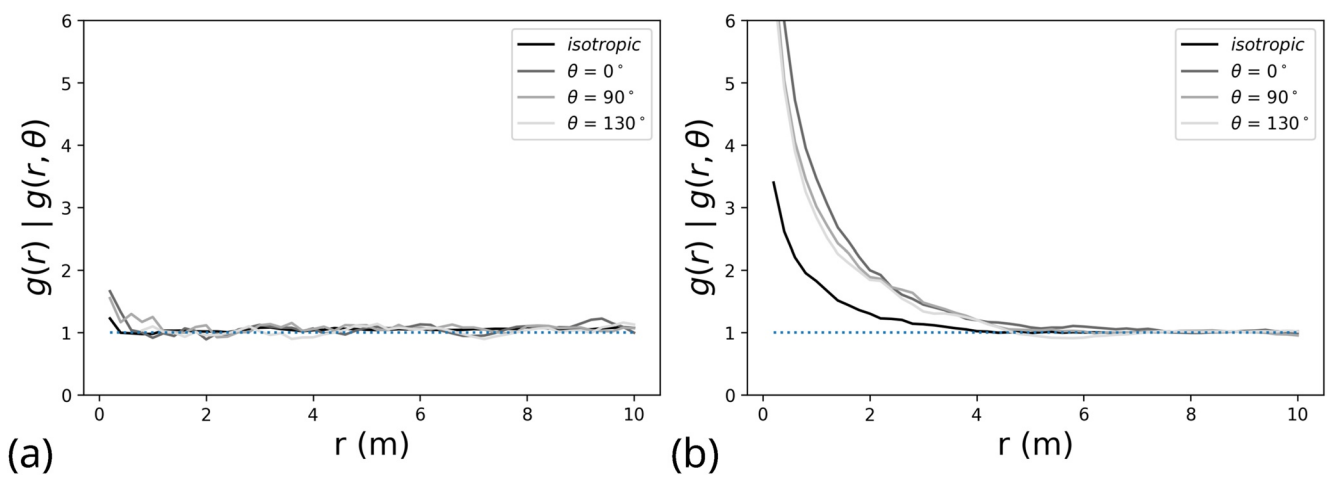

Figure 4. The empirical isotropic pcf $g(r)$ (black curve) and anisotropic pcfs $g(r, \theta)$ (gray curves) for the full set of (a) fractures and (b) branches of the artificial fracture network. Blue dotted curves indicate the theoretical value of 1.

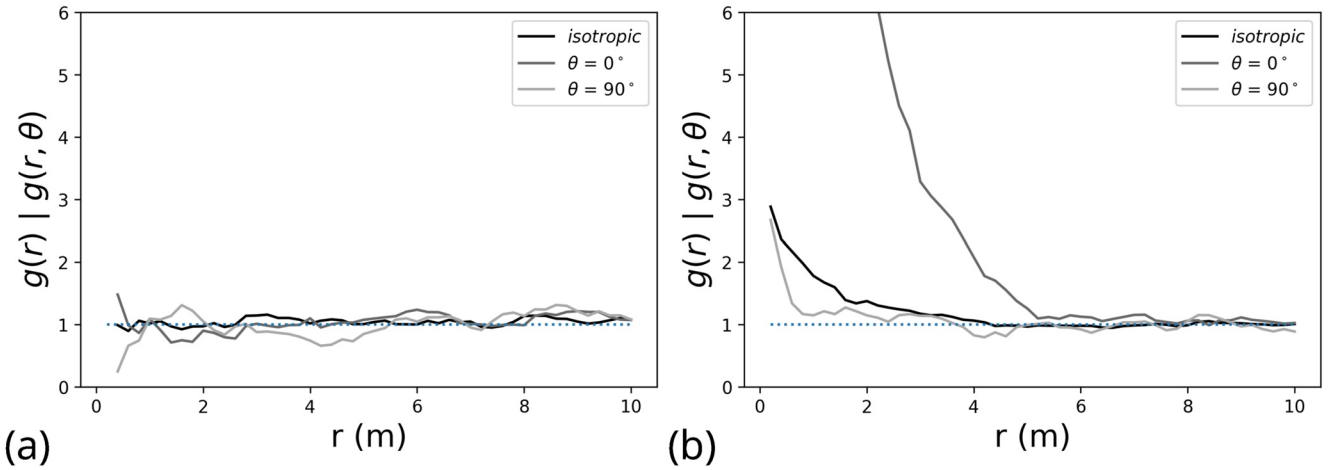

Figure 5. Empirical isotropic pcfs compared to anisotropic pcfs of (a) fractures and (b) branches of the artificial fracture network for subset N0 ($\theta = 0°$) and perpendicular objects ($\theta = 90°$).

4.2.3. Mark-Correlation Functions and Variograms

The empirical mark-correlation functions $k_{mm}(r)$ and mark-variograms $\gamma_m(r)$ for the lengths of fractures have in this artificial case a quite simple form, since the lengths of the segments are constant. Therefore, $k_{mm}(r) = 1$ and $\gamma_m(r) = 0$ for all r.

In contrast, for the branches of the artificial fracture network, the correlation functions have nontrivial forms as shown in Figure 6.

The original constant fractures were randomly divided by segment intersections, resulting in stochastic branch lengths (see Figure 3). The form of $k_{mm}(r)$ shows that nearby branches tend to have smaller lengths than the average. Indeed, short branches are frequently constructed close together, resulting from intersections of the same fracture. Note that the form of the length distribution function shows that almost 62% of branches are shorter than the mean branch length. The described correlation disappears after 5 m, which is explained by the constant fracture length.

The length variogram $\gamma_m(r)$ has relatively small values for small r, indicating that nearby branches have similar lengths, with a range of correlation of 5 m. The combined information obtained from these two correlation functions yields that nearby branches tend to be short and of similar length.

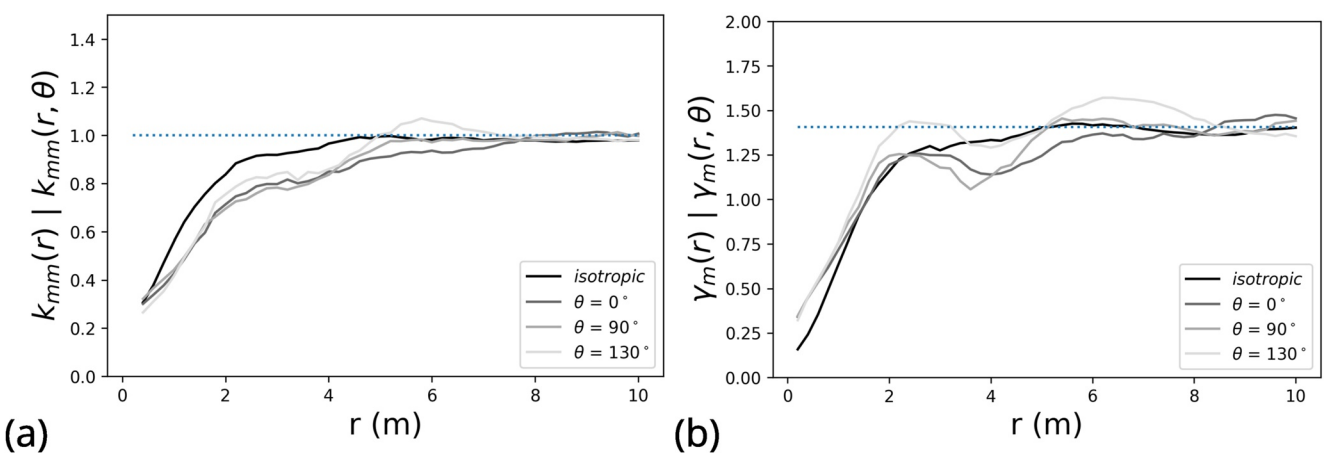

Figure 6. Empirical 0°, 90°, and 130° anisotropic and isotropic mark-correlation functions ($k_{mm}(r)$) and mark-variograms ($\gamma_m(r)$) for (a) fractures and (b) branches of the artificial fracture network. The theoretical values expected for large r are indicated by dotted blue lines.

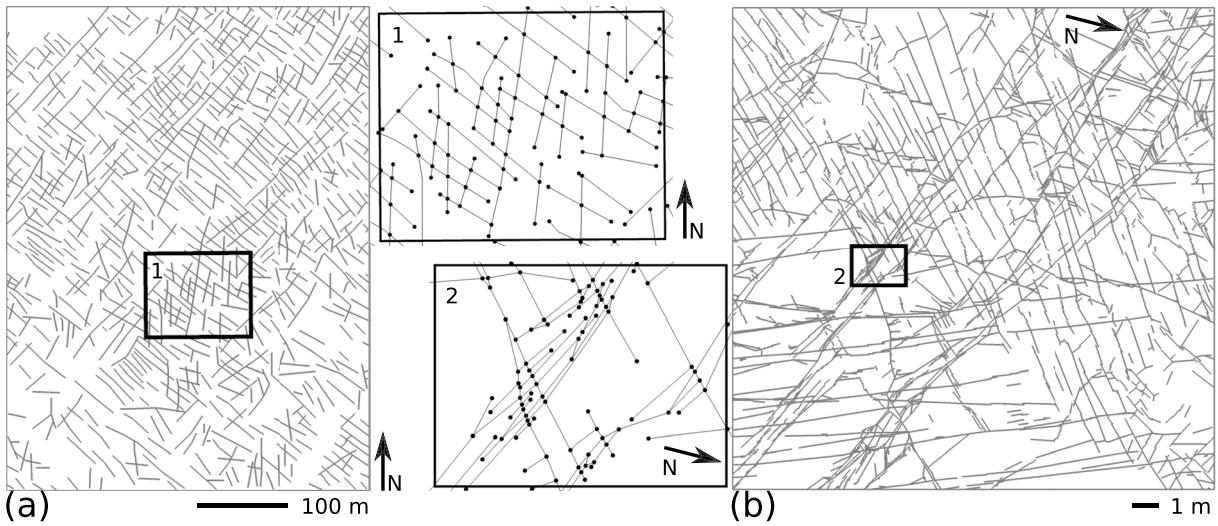

Figure 7. Natural surface exposures from (a) the southern flank of the Jabal Akhdar dome (Oman Mountains; Zeeb et al., 2013) and (b) the Hornelen basin (Norway; Odling, 1997). The central part of the figure shows enlarged views of the central parts of (1) the Oman data set and (2) the Hornelen data set. I, Y, and X nodes are marked as black dots.

4.2.4. General

For this artificial fracture network, the second-order fracture statistics reflect well the spatial behavior of a completely random collection of segments, as demonstrated by the pcfs, mark-correlation functions $k_{mm}(r)$, and mark-variograms $\gamma_m(r)$. In contrast, the results for branches are more complex. The spatial correlations result mainly from how the branches were constructed and their barycenters: they form stochastic sequences on fractures randomly scattered in space.

In the following two examples of natural fracture networks, some similar correlation functions will be observed. The above results for the case of an artificial fracture network will serve as a valuable aid and benchmark for the interpretation of natural networks.

5. Analysis of Two Natural Fracture Networks

We here analyze two natural fracture patterns. In the first, large-scale fractures were observed in a satellite image covering 120,000 m^2 of the southern flank of the Jabal Akhdar dome in the Oman Mountains. This network has been widely studied because it is typical of those in large fractured carbonate reservoirs of the Middle East (Gomez-Rivas et al., 2014; Hilgers et al., 2006; Holland, Saxena, et al., 2009; Holland, Urai, et al., 2009). The map used in this paper (Figure 7a) is from Zeeb et al. (2013).

The other fracture pattern is from the Hornelen basin in Norway. The original data set consists of seven maps digitalized at several scales by Odling (1997); we focus our investigation on the one they mapped by hand from an observation height of 4 m. This map covers 324 m^2 (18 m × 18 m; Figure 7b) and describes a small-scale fracture network with numerous small fractures. This typical joint pattern can be considered as representative of structures found in nonstratabound massive rock (Odling et al., 1999).

We chose these data sets for their complementary natures in terms of fracture pattern, scale, randomness, and variability. The Oman pattern has a spatially variable fracture density that is notably lower in the southern part (particularly for fractures striking N40). This may be considered as a weak, but acceptable, deviation from stationarity. For the Hornelen pattern, we considered only subsamples for the second-order analysis because deviations from stationarity turned out to be too strong. Both patterns are clearly anisotropic.

The centers of fractures and branches were constructed by the median rule for segments not fully within the observation window. In this analysis, we consider subsets of objects of similar orientation $\theta°$, denoted as Nθ.

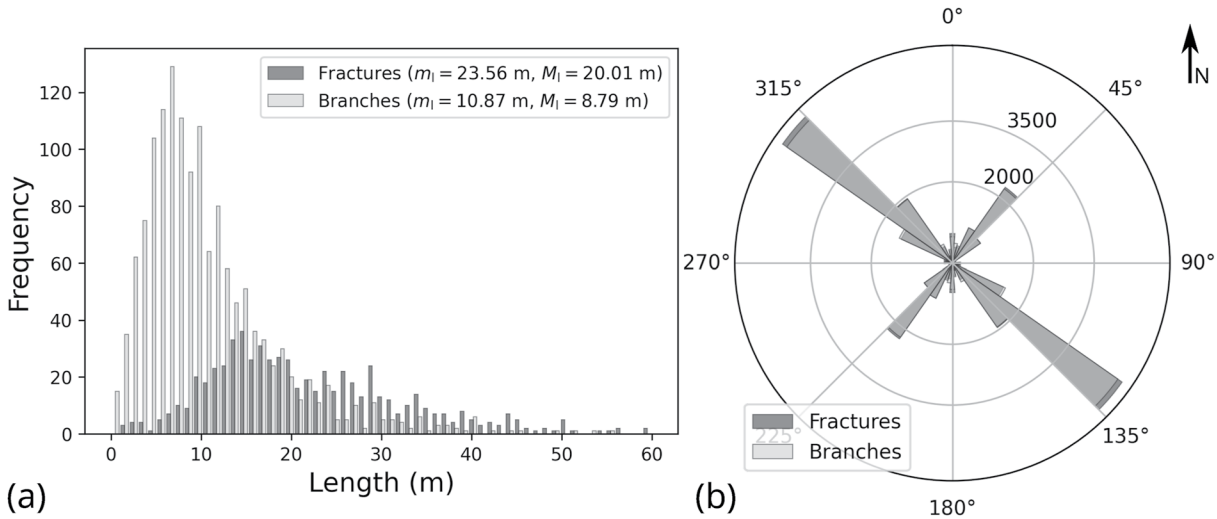

Figure 8. First-order characteristics of fractures (black) and fracture branches (gray) in the Oman exposure. (a) Length distributions (values above 60 m are not plotted); (b) rose diagram of strikes, weighted by length (per 10° interval).

5.1. Statistics for the Oman Fracture Pattern

The Oman fracture pattern (Figure 7a) was digitized using SKUA-GOCAD software. It was then analyzed using the first- and second-order methods presented earlier.

5.1.1. First-Order Characteristics

The Oman pattern was previously analyzed by Zeeb et al. (2013). Nevertheless, we studied the data again and did not obtain the exact same results; they originally identified 650 fracture traces ranging from 3 to 179 m long, whereas we identified 696 fractures with ranging from 1 to 134 m long. Furthermore, whereas Zeeb et al. (2013) reported that approximately 5% of the fractures appear to be cut by the boundary of the observation window, in our digitalization it is closer to 7%. This illustrates some impact of subjective interpretation; there is some probability that other researchers would produce distinct maps from the same data.

For an unbiased estimation of the number of fractures, we counted 663 southern endpoints of fractures in the 120,000 m^2 window. This yields an estimated fracture density of $P_{20} = 5.6 \times 10^{-3}$ m^{-2}, which is comparable to the density obtained using the 650 traces reported by Zeeb et al. (2013).

Introducing fracture branches increases the number of objects to 1,476, with lengths ranging from 0.5 to 55 m. However, this also reduced the proportion of the objects touching the boundary to approximately 4%. Note that because 40% of fractures are isolated (i.e., consisting of one branch bounded by two I nodes), 40% of the objects are the same in the fracture and branch representation. Segmentation of the other 60% of fractures leads to a density of 1.22×10^{-2} m^{-2}, an increase by a factor of 2.1.

The rose diagram (Figure 8b) was computed by weighting objects' strikes by their lengths. The results correspond well to the checkered nature of the mapped pattern, which is strongly anisotropic, with two nearly orthogonal main fracture sets oriented 40° and 130°. The fractures oriented ∼130° are quantitatively predominant. The rose diagram of branch directions is quite similar to that for fractures; the small difference is the result of approximation by segments.

Length distributions were determined for both fractures and branches (Figure 8a). Both distributions are asymmetric, with medians clearly smaller than their means. Additionally, Table 2 gives some information on the length distributions of the subsets N40 and N130. The mean fracture length of set N40 is longer than that of set N130, and fractures of set N40 are more intensively segmented, as confirmed by the smaller mean and median values of the N40 branch length distribution and the larger number of intersections per fracture C_f for N40 (2.21) than for N130 (1.11).

Table 2
First-Order Characteristics of the Oman Exposure

	Fractures			Branches		
	Full set	N40	N130	Full set	N40	N130
P_{20} (m^{-2})	0.0056	0.0015	0.0035	0.0122	0.0045	0.0064
P_{21} (m^{-1})	0.132	0.041	0.078	0.132	0.041	0.078
m_1 (m)	23.56	27.35	21.67	10.87	9.10	12.24
M_1 (m)	20.01	21.66	20.00	8.79	7.05	10.29
Connectivity						
C_f	1.42	2.21	1.11			
$p_{I\ nodes}$	0.71	0.61	0.76			
$p_{Y\ nodes}$	0.10	0.13	0.08			
$p_{X\ nodes}$	0.19	0.26	0.16			

Note that the union of sets N40 and N130 does not cover the complete fracture pattern, as a minor set comprises objects aligned north–south. However, we have neglected this minor set because it contributes only 10% of the total fracture length.

5.1.2. Second-Order Characteristics

5.1.2.1. Pair-Correlation Functions: All Fractures

Figure 9 shows the empirical isotropic pcf and two anisotropic pcfs for the entire pattern of fractures and branches. The directions investigated for the anisotropic pcfs $g(r, \theta)$ are the two main orientations, $\theta = 40°$ and 130°.

The isotropic and 130° pcfs for fractures (Figure 9a) do not deviate significantly from 1, that is, the case of a completely spatially random distribution of segment barycenters. However, the 40° pcf shows three clear maxima at $r = 6.5$, 13, and 19.5 m. The first indicates the abundance of similar intercenter distances of ∼6.5 m, and thus some degree of short-range order; the second and third maxima may be seen as weak traces of long-range order (see Appendix C for explanations of "short-range order" and "long-range order").

The pcfs for branches (Figure 9b) clearly differ from those for fractures. They have forms typical of the pcfs of point processes with short-range order: that is, all have a clear single maximum, which is around $r = 5.5$ m in the isotropic case and for $\theta = 40°$, but around $r = 8.5$ m for $\theta = 130°$.

This behavior can be explained by the checkered nature of the network. A given fracture is typically intersected by other, nearly orthogonal fractures, and these intersection points (i.e., branch ends) form nearly regular sequences. Consequently, the branch barycenters also form nearly regular sequences, leading to the observed form of the pcf. Because the intersection points do not form irregular sequences like in the artificial fracture network (Section 4), there is no motive to think about a pole at $r = 0$. The r-value at which the maximum occurs gives information on typical (frequent) interpoint distances, which are related to branch lengths, and on the sizes of intact rock blocks. The different values of the maxima of the pcfs, that is, $g(5.5, 40) = 2.7$ and $g(8.5, 130) = 1.7$ (Figure 9b), characterize the different strengths of order in the two directions: branch centers are more regularly spaced along $\theta = 40°$ than 130°.

To obtain more detailed second-order information, we now refine our analysis by identifying the separate contributions of sets N40 and N130 to the anisotropic pcfs.

5.1.2.2. Pair-Correlation Functions: Set N40

Figure 10 shows the isotropic and anisotropic pcfs for fractures and branches in the set N40. Whereas the isotropic pcfs have forms similar to those in the case of complete spatial randomness (i.e., with no major peaks), the

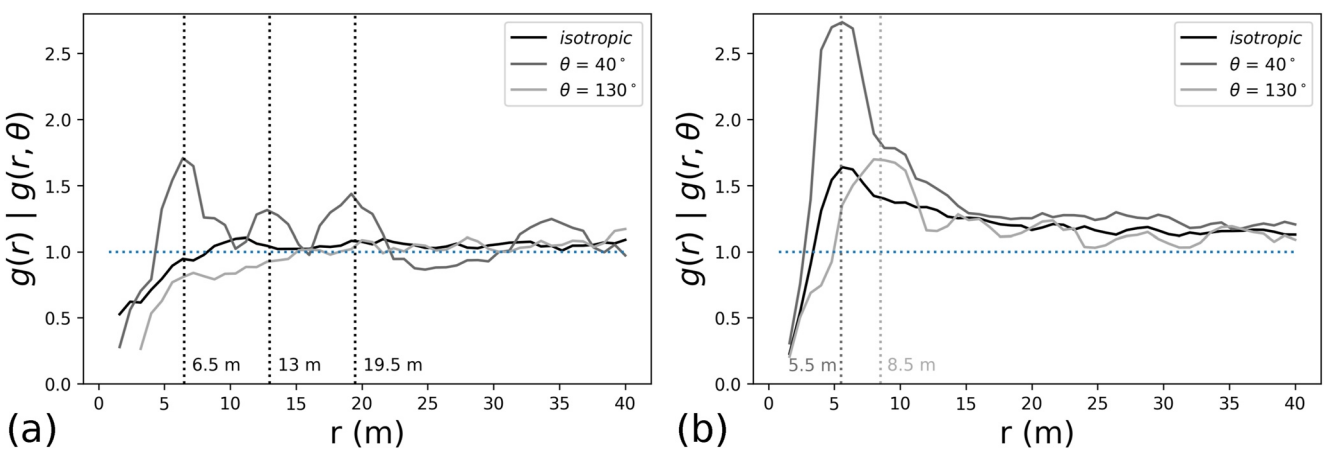

Figure 9. Isotropic (black curve) and anisotropic pcfs (gray curves) for the full set of (a) fractures and (b) branches in the Oman data set.

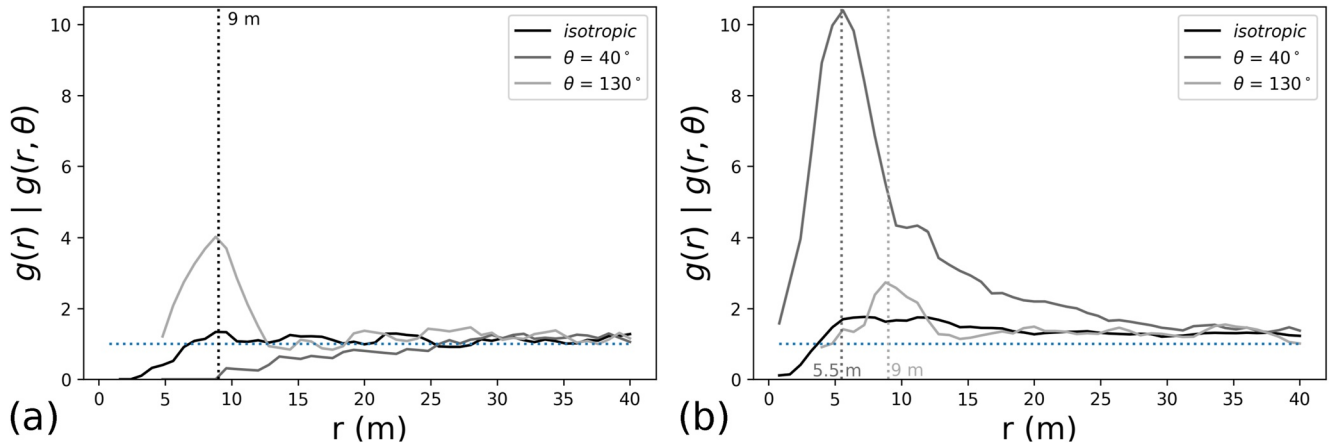

Figure 10. Empirical isotropic and anisotropic pcfs for (a) fractures and (b) branches in subset N40 of the Oman data set.

anisotropic pcfs show interesting structural features indicating clear differences between the spatial organization of fractures and branches.

In the orthogonal direction $\theta = 130°$, the pcfs $g(r, 130)$ for N40 fractures and branches indicate weak short-range order, with a maximum at $r = 9$ m (Figure 10). This reflects the regular spacing between N40 fractures.

In the main direction of orientation $\theta = 40°$, $g(r, 40)$ for fractures indicates repulsion until $r = 25$ m, then disorder (Figure 10a). The N40 fractures are aligned, and the repulsion between fracture centers (which causes $g(r) < 1$) in their direction of alignment reflects the fact that, within a certain distance of a fracture center along its direction of alignment, any fracture one is likely to find is probably an extension of the same fracture.

In contrast, the maximum of the pcf $g(r, 40)$ for branches at $r = 5.5$ m indicates a high degree of short-range order (Figure 10b). The shape of the curve is similar to that in Figure 9b: the maxima are at the same position ($r = 5.5$ m), but the value of the maximum here is 10.5, compared to 2.7 in Figure 9b. There may even be a second maximum at $r = 11$ m, suggesting some degree of long-range order. This suggests that the branches of set N40 account for the dominant contribution to Figure 9b, probably because N40 fractures are longer and comprise more branches than N130 fractures. This behavior statistically reflects the obvious order of arrangement along $\theta = 40°$, which is caused by nearly equidistant intersections by N130 fractures.

5.1.2.3. Pair-Correlation Functions: Set N130

The pcfs corresponding to subset N130 (Figure 11) have forms similar to those of subset N40, but with lower maxima, indicating a lower degree of order (note the different y-axis scales in Figures 10 and 11).

Fractures in set N130 are responsible for the order observed along $\theta = 40°$ in Figure 9a. Indeed, the pcf $g(r, 40)$ for N130 fractures indicates weak short-range order (indicated by the maximum at $r \approx 6.5$ m). This is related to both the nearly regular spacing of N130 fractures and the alignments of their centers along $\theta = 40°$. Along $\theta = 130°$, the $g(r, 130)$ curves show repulsion between fracture centers until $r = 22$ m, and then irregular fluctuations around 1. The N130 fractures are thus aligned, but fracture centers are not near to each other in the direction $\theta = 130°$.

For branches, the $g(r, 130)$ curves have maxima at $r = 7.5$ and 15 m, but the maxima are again smaller (3.5 at $r = 7.5$ m and 1.6 at $r = 15$ m) than those for N40. Interestingly, the curve for the alignment of branches in the orthogonal direction (40°) indicates order, with maxima of 2 at $r = 7.5$ m and 1.5 at $r = 15$ m. Thus, the centers of N130 branches tend to be aligned and regularly spaced along both $\theta = 40°$ and 130°.

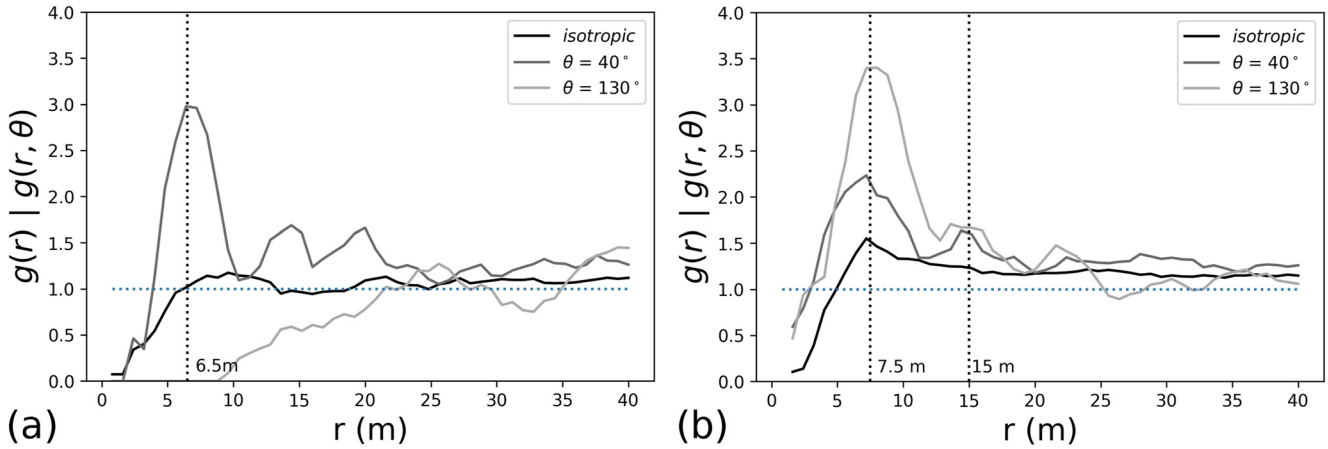

Figure 11. Empirical isotropic and anisotropic pcfs for (a) fractures and (b) branches in subset N130 of the Oman data set.

5.1.2.4. Pair-Correlation Functions: Lengths and Spacing

Although analyzing fracture branches in the artificial fracture network was of questionable utility, this same exercise yields interesting statements about the organization of the Oman fracture network. Indeed, due to its checkered nature, branches can be considered its most basic components.

Our separate analyses of the N40 and N130 fracture sets show that the maxima of branch pcfs occur at similar intercenter distances in both sets; depending on the set and direction considered, the obtained forms are related to the lengths of branches and thus to the spacing between fractures. The higher degree of order shown by branch centers of the N40 fracture set in the direction $\theta = 40°$ results from long sequences of regularly spaced branch centers. Indeed, N40 fractures are quite long and intensively segmented by regularly spaced N130 fractures.

Unlike the artificial network, the natural networks contain Y nodes (Table 2) which give an indication of the relative ages of the different fracture sets. Thirty-seven percent of N40 fractures end on N130 fractures, whereas only 22% of N130 fractures abut on N40 fractures. Following kinematic principles, this means that the N40 fractures tend to be older. Therefore, the sizes of N130 fractures are bounded, creating a certain degree of alignment of the nearly regular N130 fracture centers.

The pcfs $g(r, 40)$ for the N40 fractures and $g(r, 130)$ for the N130 fractures reveal another aspect of fracture organization: repulsion between fracture centers, which also impacts mean fracture length. This highlights how little interaction occurs between fractures of the same set.

5.1.2.5. Mark-Correlation Functions and Variograms

Perhaps surprisingly, the empirical mark-correlation functions and mark-variograms for fractures (Figure 12a) show a behavior broadly similar to that of the artificial network (Figure 6a), that is, ignoring small statistical fluctuations and deviations from the theoretical values in the case of independent marks. Thus, one may conclude that the length marks are independent. This differs from the result of Bour (2002) that "small faults are more clustered than large ones," in which case the mark-correlations would be similar to those for fracture branches (Figure 12b). In nature, both situations, that is, spatially correlated and uncorrelated fracture lengths, probably occur (see also the mark-correlation function in Figure 17a). Unfortunately, statistical methods for proving significance statements in this context have not yet been developed.

The empirical mark-correlation functions $k_{mm}(r)$ for branches are shown in Figure 12b. They indicate spatial correlations of length marks that can be easily interpreted. Nearby branches (within ∼30 m) tend to be shorter than the average branch length, a clear difference compared to fractures. The empirical length variograms $\gamma_m(r)$ (Figure 12b) also indicate that nearby branches (again within ∼30 m) are of similar length. Combined, this information demonstrates that nearby branches tend to be both short and of similar length. This is plausible due to the construction and regular spacing of branches, as described above.

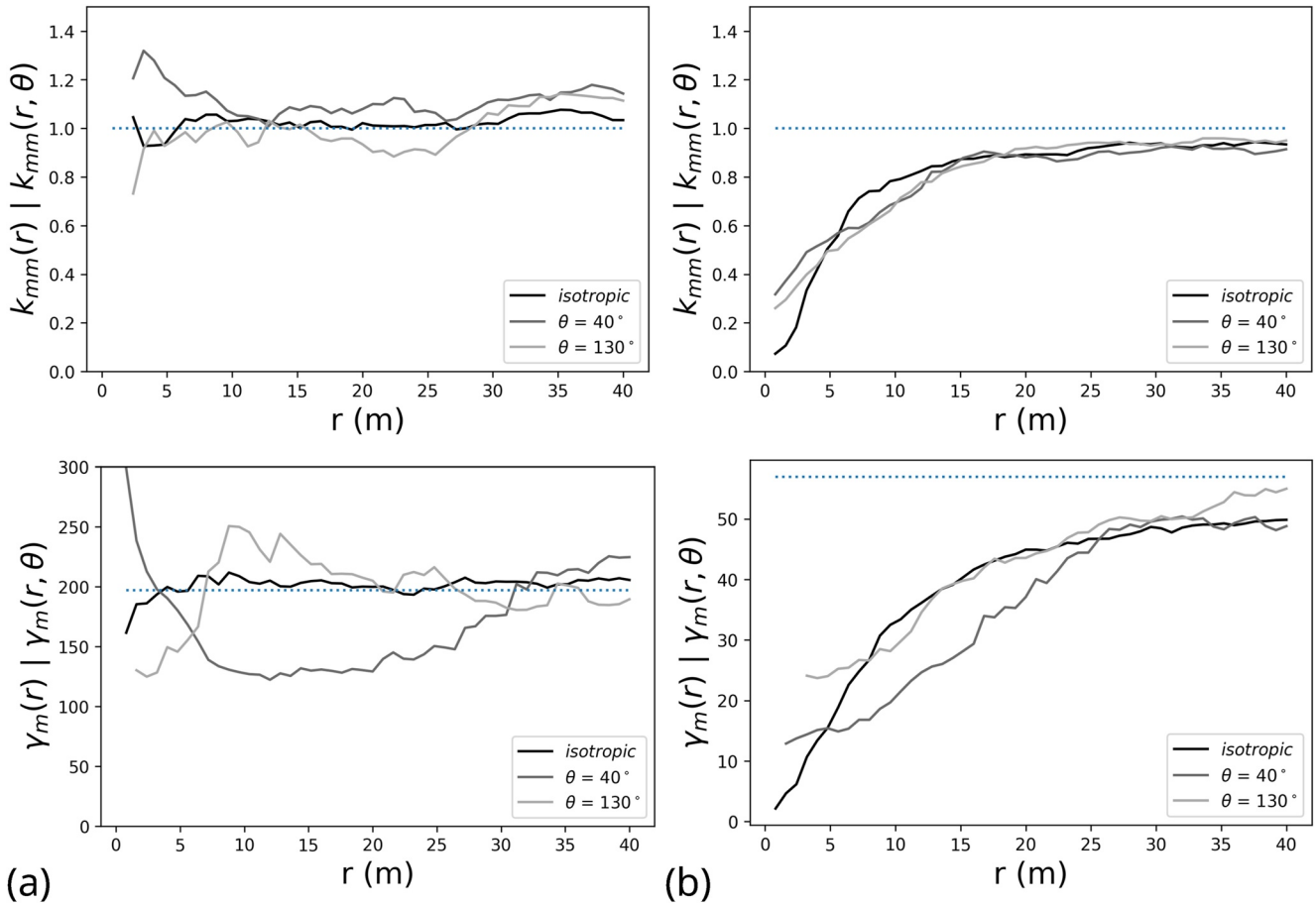

Figure 12. Empirical length mark-correlation functions $k_{mm}(r)$ and length mark-variograms $\gamma_m(r)$ for (a) fractures and (b) branches of the Oman exposure. The theoretically expected values for large r or in the case of independence are shown as dotted blue lines.

5.2. Statistics for the Hornelen Fracture Pattern

5.2.1. First-Order Characteristics

The map in Figure 7b contains 2,109 fractures with lengths ranging between 1 cm and 11.0 m, with 5.4% of the fractures being cut by the boundary. Introducing the branch representation increases the number of objects to 4,350 and reduces the range of object lengths to 1.1 mm to 5.6 m and the proportion of objects cut by the boundary to 2.6%.

We counted 2,033 southern endpoints of fracture in the 324 m^2 window. Thus, the edge-corrected count yields an estimated fault density $P_{20} = 6.27\ m^{-2}$. Isolated fractures account for 60% of the fractures in the observation window, and segmentation of the other 40% leads to a branch density of 13.18 m^{-2}, almost twice the fracture density.

The network consists of three main fracture sets oriented ∼50°, ∼130°, and ∼170°. We note that Odling (1997) reported the orientation of the third fracture set to be 0° (=180°) based on consideration of a larger area. The rose diagram of branch strikes is, as expected, similar to that for the fractures (Figure 13b).

Here, we use the same statistical analysis as for the Oman data set, but for three sets of fractures (N50, N130, N170). As for the Oman data set, a small part of the total length of the network (9.6%) is not represented by these three subsets.

Stronger deviations from stationarity appear when considering these three subsets (Figure 14a). Indeed, the spatial densities of sets N130 and N170 are greater in the center and southeast of the exposure, respectively (green and red, respectively, in Figure 14a). Both sets have rather long fractures. In contrast, set N50 (blue in

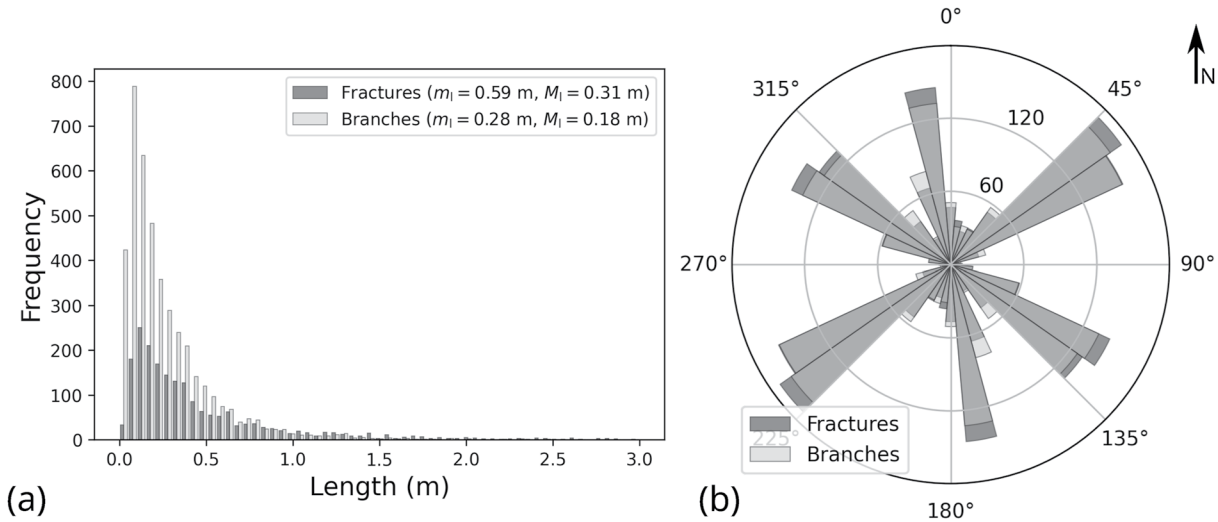

Figure 13. First-order characteristics of fractures (black) and fracture branches (gray) in the Hornelen exposure. (a) Length distributions (values above 3 m are not plotted). (b) Rose diagram of strikes weighted by length (per 10° interval).

Figure 14a) is more diffuse and contains smaller and more isolated fractures. Therefore, we defined the subwindows shown in Figure 14a and performed statistical analyses of each subset, assuming stationarity, only in its respective subwindow.

The empirical length distributions are asymmetric (Figure 13a), consistent with the findings of Odling (1997), who fitted a log-normal distribution to the fracture lengths in this exposure. The length distributions of branches of the three subsets are presented in Table 3 and Figure 14b.

The connectivity measures reveal that the average number of connections per fracture in set N130 is higher than those for sets N50 and N170. The abundance of small fractures in set N50 may explain its low connectivity index.

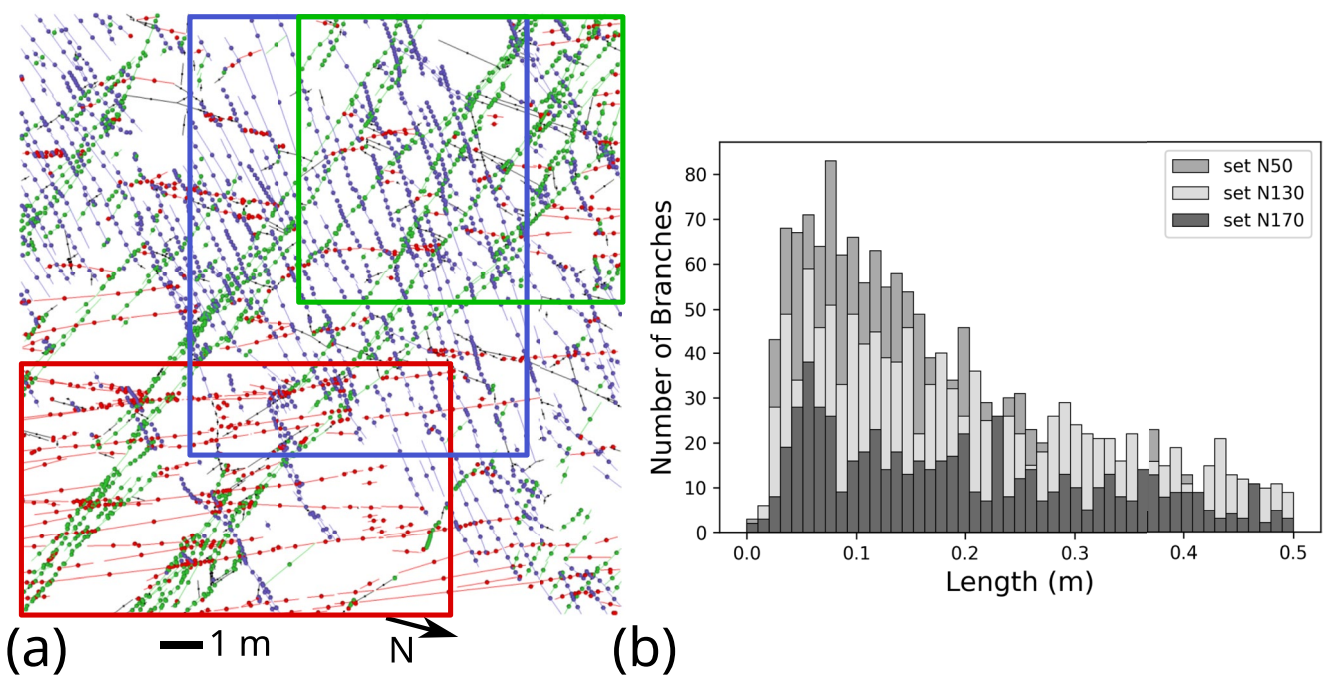

Figure 14. Hornelen surface exposure. (a) Map of branch centers, with branches of the N50, N130, and N170 subsets shown in blue, green, and red, respectively, and other branches in black. Statistical analyses for these three sets were performed only within the indicated subregions. (b) Length distributions of the N50, N130, and N170 subsets (in dark gray, light gray, and black, respectively), focusing on branches 0–0.5 m long.

Table 3
First-Order Characteristics of the Hornelen Exposure

	Fractures				Branches			
	Full set	N50[a]	N130[a]	N170[a]	Full set	N50[a]	N130[a]	N170[a]
P_{20} (m^{-2})	6.27	3.75	1.90	1.85	13.20	6.88	5.61	4.10
P_{21} (m^{-1})	3.68	1.50	1.43	1.72	3.69	1.51	1.44	1.72
m_1 (m)	0.59	0.47	0.82	1.05	0.28	0.24	0.26	0.44
M_1 (m)	0.31	0.23	0.43	0.37	0.18	0.16	0.19	0.23
Connectivity								
C_f	1.76	1.15	2.60	1.92				
$p_{I\ nodes}$	0.60	0.74	0.50	0.57				
$p_{Y\ nodes}$	0.29	0.16	0.35	0.27				
$p_{X\ nodes}$	0.11	0.10	0.15	0.16				

[a]Statistics for each subset were calculated for their respective subwindows in Figure 14a.

5.2.2. Second-Order Characteristics

5.2.2.1. Pair-Correlation Functions: All Fractures

The isotropic pcf for all fracture centers within the observation window (Figure 15a) indicates weak short-range order with the most frequent intercenter distance being 8 cm. The anisotropic pcf for $\theta = 50°$ indicates weak short- and long-range order with maxima at $r = 8$ and 24 cm, respectively. This may be explained by the sequences of en echelon fractures observed in the N50 fracture set. For $\theta = 130°$ and 170°, the pcfs indicate complete spatial randomness.

For fracture branches, the pcfs indicate some degree of clustering. As with the artificial fracture network, this results from random sequences of branch centers focused on fractures.

5.2.2.2. Pair-Correlation Functions: Subsets of Fractures

We now present empirical isotropic and anisotropic pcfs separately for the N50, N130, and N170 subsets. As with the Oman data set, in the anisotropic pcfs, we investigate the directions defined by the dominant strike of the subset (dark gray curves in Figure 16) and its perpendicular (light gray curves in Figure 16).

Fractures of the subsets N130 and N170 are similarly distributed. In their dominant directions, anisotropic pcfs indicate some weak long-range order with two maxima at $r = 16$ and 32 cm for $\theta = 130°$ (Figure 16a, N130) and at 25 and 50 cm for $\theta = 170°$ (Figure 16a, N170). The fractures in these sets are regularly aligned along strike. In contrast, perpendicular to strike, the pcfs fluctuate around 1, as is typical in the case of complete randomness.

The anisotropic pcf along $\theta = 50°$ for fractures in the set N50 indicates short-range order, with the most frequent intercenter distance being $r = 18$ cm. However, a higher degree of short-range order is shown by the pcf $g(r, 60)$ at the same intercenter distance, but in the slightly oblique direction $\theta = 60°$ (Figure 16a, N50): at $r = 18$ cm, $g(r, 60) = 12$, whereas $g(r, 50) = 4$. This alignment of fractures in a direction slightly oblique to their strike is characteristic of the previously mentioned en echelon fractures. We also note randomness perpendicular to strike.

For fracture branches, the along-strike pcf curves for both the N130 and N170 subsets indicate clustering of branch centers. This situation looks broadly similar to that of the artificial fracture network, but with a subtle difference: the degree of clustering is obviously higher than that for fractures. This is because the branch centers are clustered on fracture traces and are not random (Poisson-process-like) as in the case of the artificial network.

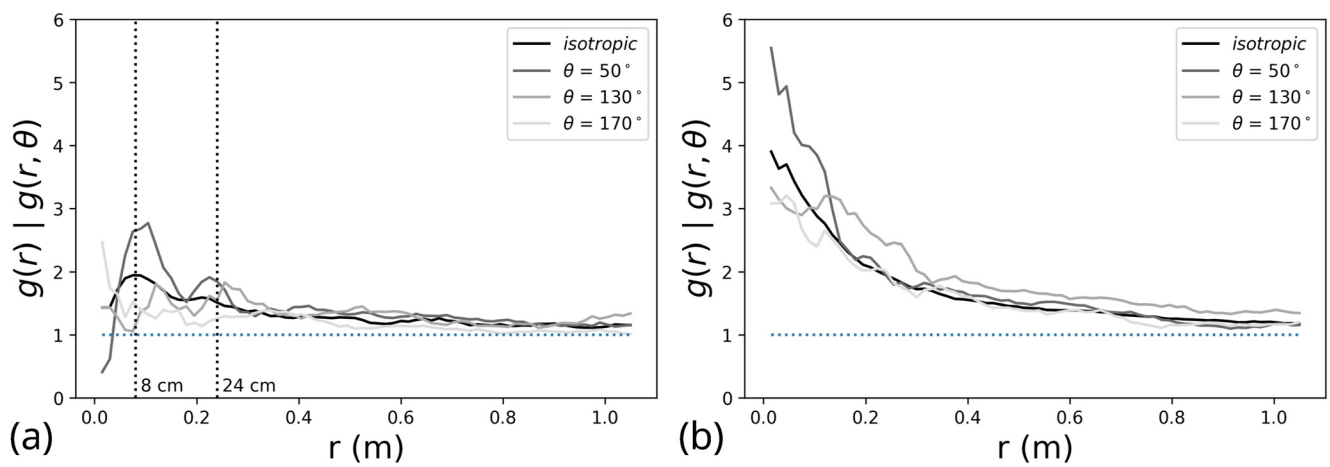

Figure 15. Isotropic and anisotropic pcfs (black and gray curves, respectively) for (a) the full set of fractures and (b) the full set of branches in the Hornelen exposure.

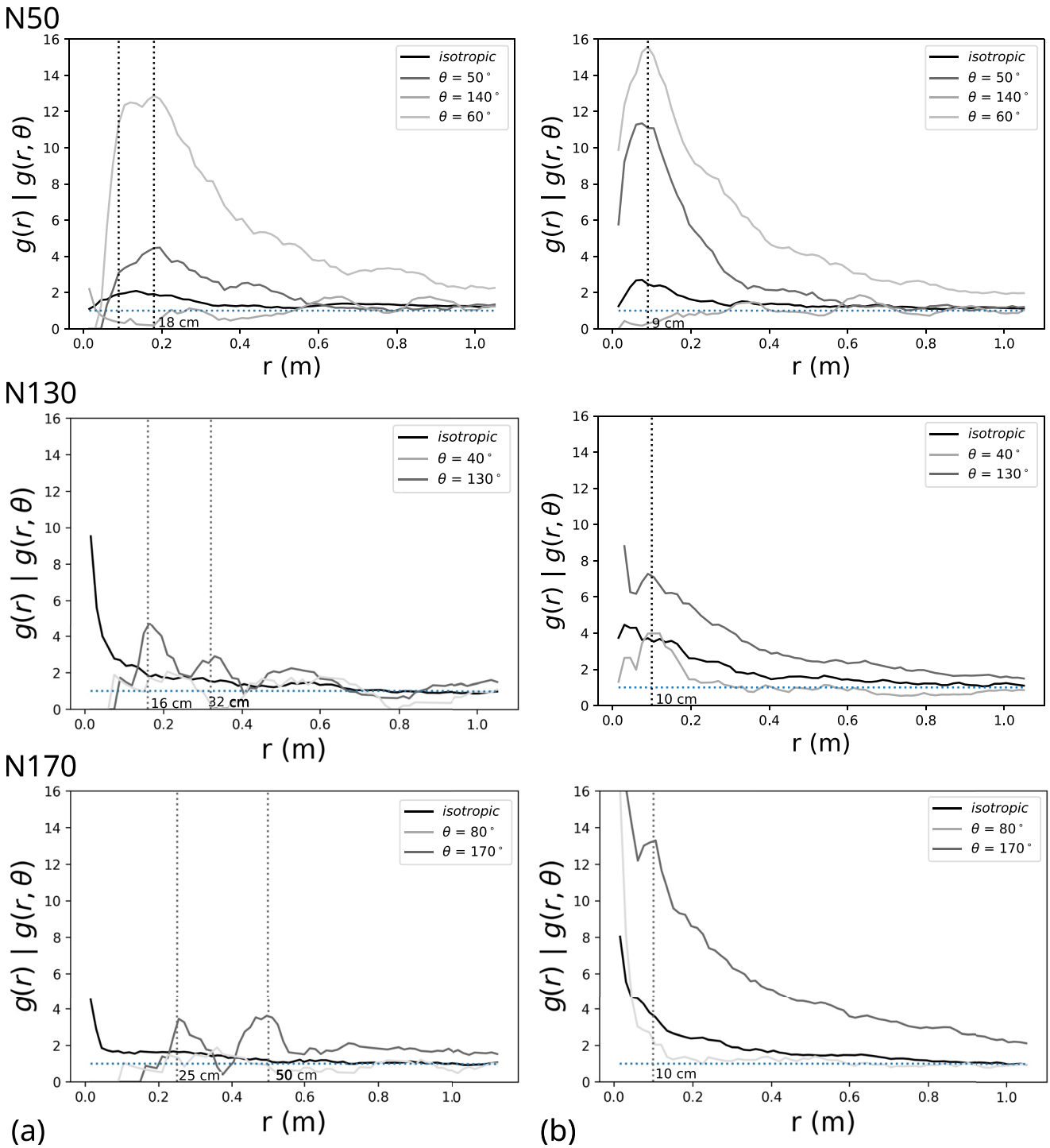

Figure 16. Empirical isotropic and anisotropic pcfs for (a) fractures and (b) branches of the subsets N50, N130, and N170 in the Hornelen data set.

The pcfs for branches in the N50 subset show short-range order with maxima at $r = 9$ cm in the directions $\theta = 50°$ and 60°. This probable interpoint distance of 9 cm is half of the value measured for N50 fractures. This is consistent with the small connectivity index of 1.15 intersections per fracture (Table 3), which suggests that N50 fractures are often divided in two. Inspection of Figure 14a confirms that N50 fractures (blue) are typically intersected by N130 fractures (green). Furthermore, the $g(r, 40)$ pcf for N130 fracture branches (i.e., perpendicular to strike) shows some degree of short-range order with a maximum at $r = 10$ cm. Thus, the spacing of N130 fractures is related to the segmentation of N50 fractures.

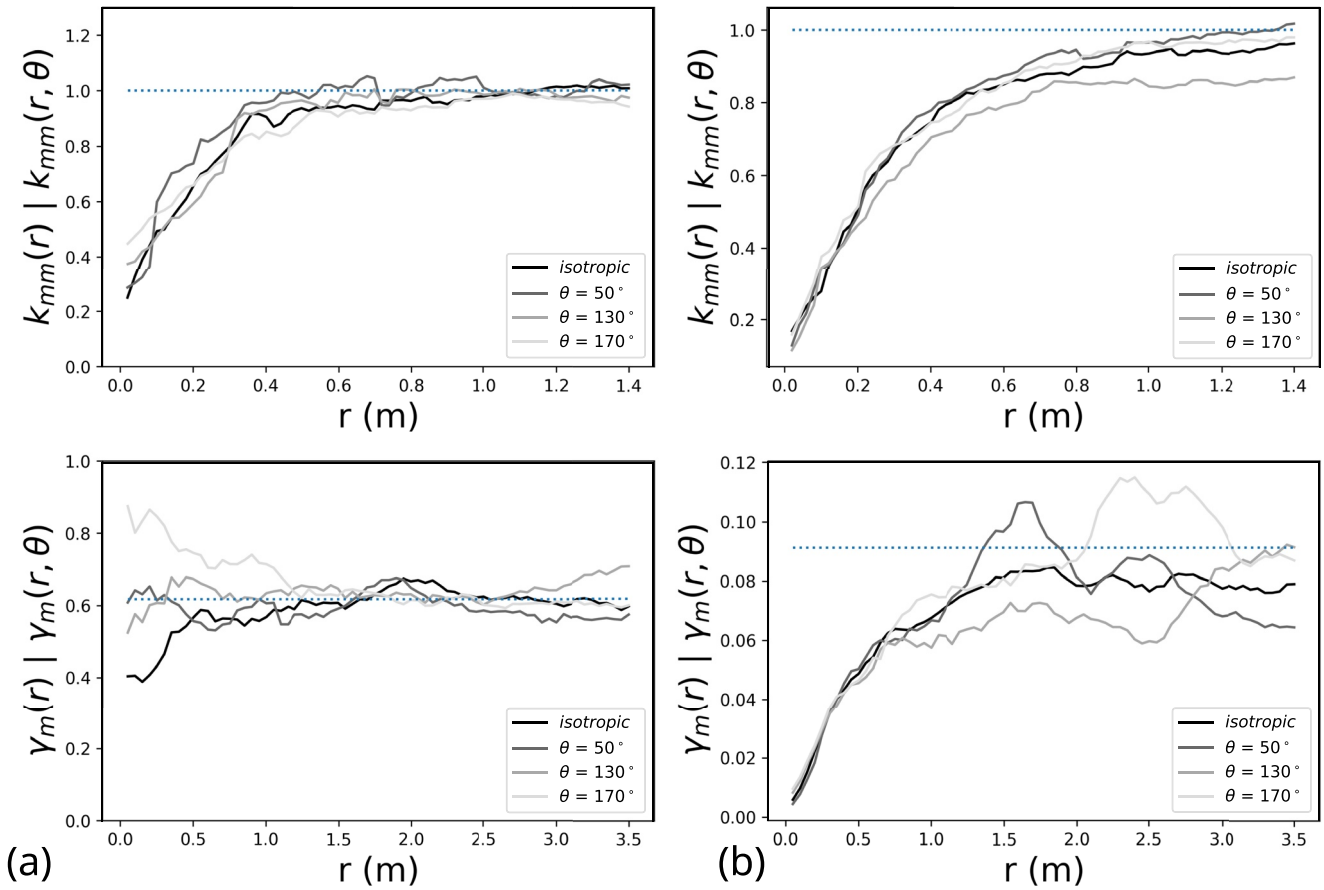

Figure 17. Empirical length mark-correlation functions $k_{mm}(r)$ and variograms $\gamma_m(r)$ for (a) fractures and (b) branches in the Hornelen outcrop. Theoretical values for large r are shown as dotted blue lines.

5.2.2.3. Mark-Correlation Functions and Variograms

The empirical isotropic and anisotropic mark-correlation functions and variograms for the branches of the Hornelen data set (Figure 17b) reveal a similar form to the spatial correlation as in the Oman data set (Figure 12b), but at quite different length scales and ranges of correlation.

In contrast, for fractures, the results from the Oman data set show more random behavior, whereas the Hornelen data set (Figure 17a) shows some inhibition of fracture lengths at short distances (up to 0.6 m), and the mark-variogram indicates a tendency toward similar lengths up to 0.5 m. Combined, this information indicates that nearby fractures and branches in the Hornelen data set tend to be short and of similar length.

More precisely, we here consider a randomly chosen pair of fractures with lengths l_1 and l_2 and an intercenter distance r. Let the mean of all products $l_1 \cdot l_2$ be $m(l_1 l_2)$, and the mean fracture length for all fractures be m_1. Then:

$$k_{mm}(r) = \frac{m(l_1 l_2)}{m_1^2}. \tag{7}$$

The curves in Figure 17a for $k_{mm}(r)$ can then be approximated as

$$\begin{cases} k_{mm}(r) = 0.2 + \sqrt{r} \text{ for } r \le 0.6\,\text{m} \\ k_{mm}(r) = 1 \text{ for } r > 0.6\,\text{m}. \end{cases} \tag{8}$$

This shows that nearby fractures (closer than 0.6 m) tend to be shorter than the average fracture length because the mean of the corresponding lengths is smaller than the square of the overall mean length.

This result can be compared with the findings of Darcel et al. (2003a), who studied nearest-neighbor correlations in the seven maps of the Hornelen data set; this statistical approach is an alternative to second-order methods. Their main finding was that the average distance $d_c(l)$ between the barycenter of a fracture of length l and that of its nearest neighbor depends weakly on l as $d_c(l) \sim l^{0.3}$ for small l, but is independent of l for larger l, as expected for independent length marks.

5.3. Comparison of the Oman and Hornelen Fracture Networks

The analysis in Sections 5.1 and 5.2 highlights various clear differences between the two fracture networks. Whereas the Oman fracture network is clearly anisotropic, with two almost perpendicular dominant orientations, the Hornelen network shows directional disorder, with three dominant directions; indeed, this pattern shows so much variability that we had to consider three subsets to achieve an acceptable second-order analysis.

The most obvious aspect of the organization of the Oman fracture network is its strong regularity, that is, the regular spacing of fractures in both the N40 and N130 subsets. This regularity is probably due to bed thickness; relationships between fracture spacing and bed thickness have been discussed for stratabound fracture networks (e.g., Ji et al., 1998). However, the anisotropic pcfs orthogonal to fractures provide interesting complementary information about order and the most frequent interfracture distances. For the subset N40, there is short-range order with a most frequent interfracture distances of 9 m. For the subset N130, there is even some degree of long-range order with a smaller most frequent interfracture distance of 6.5 m (Figures 10 and 11). The maxima of the pcfs occurred at values of r determined by the modes of the branch lengths, as is to be expected from the checkered nature of this network. Analyzing branches thus yielded clearer information than analyzing the fractures themselves.

The N40 fracture set tended to comprise older fractures that stopped N130 fractures. This relative chronology limits the size of N130 fractures and tends to align their centers along $\theta = 40°$. The 40° anisotropic pcf for N130 fractures captures this additional aspect of regularity as long-range order. Therefore, the methodology presented herein is able to characterize not only fracture spacing, but the chronology of the fracturing process, which may prove useful in refining our understanding of the links between fracturing and stratigraphy in stratabound fracture networks.

In contrast to the Oman fracture network, all subsets of the Hornelen network show high degrees of variability in their fracture spacing. Here, our second-order analysis using branches was not as helpful as for the Oman network. However, it indicates some similarity with the artificial fracture network, albeit with higher local variability: whereas branch centers sampled a one-dimensional Poisson process in the artificial network, fractures were clustered in the Hornelen network, increasing the strength of the pcf poles. In contrast to the Oman network, the Hornelen fractures, not the branches, seem to hold more interesting information in the second-order analysis.

The along-strike anisotropic pcfs for fractures indicate interesting aspects of order in both fracture networks. In the Oman network, they reveal a weak repulsion between fractures at distances shorter than the mean fracture length, and disorder at greater distances. This indicates that fractures of both Oman subsets do not overlap and that very few fractures of the same subset interact.

In the Hornelen fracture network, in contrast, the N130 and N170 subsets show some degree of long-range order (at least, within their respective subwindows), whereas the N50 subset seems to possess only short-range order. The N130 and N170 fracture centers are regularly aligned along their strikes, whereas the N50 fracture centers are not (Figure 16a, N50), most likely because of the large proportion of en echelon fractures in that orientation. This suggests that the N50 fractures developed via interactions and connections of small fractures, where larger fractures probably drove the development of smaller ones at their tips (de Joussineau & Aydin, 2007; Segall & Pollard, 1980).

6. Discussion

We used the marked point process or object model approach, taking linear segments as marks or objects representing fractures and fracture branches. These segments are characterized by lengths and azimuthal directions. Thus, there is basically no loss of information, although in the point process analysis, we ignored intersections and tips. More complex objects can be considered by adding more marks such as aperture, displacement, or connectivity type.

The "points" in this and previous works (e.g., Bonnet et al., 2001) are geometrically defined as segment barycenters. This seems appropriate because we consider surface exposures, essentially planar sections through three-dimensional fracture systems, where physically defined points (e.g., nucleation points) are positioned somewhere within the rock's interior. Even with full knowledge of the geometry of three-dimensional samples, it remains complicated to detect such points.

The "marks" used are lengths and directions. The directional marks appear only in forming the sets of fractures. They could be used for studies of local parallelity of fractures, using ideas from Illian et al. (2008), Section 5.4.

An important question in the statistical characterization of fracture networks is which objects should be used in the point process approach: fractures or branches? On one hand, fractures are primary objects holding geological information. However, fractures can be quite long and their barycenters may have little to do with their full appearance. This is particularly true when fracture lengths span several orders of magnitude. On the other hand, branches are constructed or secondary objects subdividing fractures according to their intersections. However, branches have some topological meaning and capture information about connectivity. Therefore, the use of branches may sometimes be a good compromise for variability and correlation analyses.

In concrete applications, it probably makes sense to study fractures and branches in parallel, at least until some tendency in the data indicates one to be more useful. For instance, in well-developed and highly connected fracture networks, branches may be considered the main constitutive geometrical elements and thus offer more interesting information. If, in contrast, a network contains many isolated (e.g., en echelon) fractures, information on connectivity may be of little interest, and an analysis of fractures may be preferable. The Hornelen data set includes both long, interconnected fractures and small, isolated fractures. These different configurations may require separate analyses to better understand the relationship between "poorly developed" (also known as "unsaturated" or "dilute") and "well-developed" ("saturated" or "dense") components (Davy et al., 2010; Josnin et al., 2002; Wu & Pollard, 1995).

We have shown that the isotropic pcf $g(r)$ is not sufficient for analyzing fracture networks by point process methods. Because fracture networks are strongly anisotropic structures, we are convinced that the anisotropic pcf $g(r, \theta)$ is a crucial tool for quantifying the inner organization of fracture networks.

Relations such as Equation 8 and its nearest-neighbor counterpart are probably only valid for special fracture networks. Only further research on many various fracture networks may lead to general statements and a deeper understanding of their organization. We remark here that, in general point process statistics, nearest-neighbor statistics is a good alternative to second-order methods.

When defining fracture branches, nodes are of particular interest. Indeed, nodes contain vital information about (a) relationships between fractures (abutting/cross-cutting), (b) potential stress concentrations and interactions, and (c) the relative timing of fracturing. This remains true in the planar case. Systematic studies of node-related statistics may therefore prove fruitful in the future.

We now highlight an alternative approach to the statistical analysis of fracture networks, which uses ideas from the theory of "segment processes" (Chiu et al., 2013, Chapter 8; Stoyan, 2021). In this context, the entire fracture network is considered as a sample of a random collection of straight-line segments. In contrast to the object model approach, the segments are not considered individual entities; this approach only counts their contribution to the planar distribution of the total segment length. Then, one is free of the need to define individual objects and their location points. The fracture intensity P_{21} and the rose diagram, both characteristic of a long tradition in fracture network statistics, can be seen as belonging to the segment-process approach. However, we do not recommend the segment-process approach because of difficulties in the corresponding second-order theory (see Chiu et al., 2013, p. 330).

Obviously, the Boolean segment process with Poisson-process centers is too simple a model for the realistic stochastic modeling of fracture networks. Nevertheless, our results for both the Oman and Hornelen fracture networks show that better models may be developed from similar Boolean processes. Indeed, the pcfs of fracture barycenters in Figures 9a and 15a are similar to the simple form $g(r) \equiv 1$ that is true for a Poisson process. Perhaps, then, realistic models may be developed using other point processes.

7. Conclusions

Advanced statistical methods for planar point processes provide a quantitative description of the variability and inner correlations of fracture networks. Here, we present the tools for such analyses; they are based on constructed marked points that represent fractures or fracture branches, collectively called "objects."

There is no a priori criterion for whether one should work with fractures or fracture branches. One should consider both the degree of fracture connectivity and the proportion of isolated fractures. A safe recommendation is to use both objects in parallel for the same network because of the complementarity of the information obtained: analyzing fractures provides a quantitative description of their hierarchical organization, whereas analyzing fracture branches describes fracture spacing and segmentation.

We performed a second-order analysis of a simple artificial fracture network, a Poisson–Boolean segment process, to test our methods under ideal conditions. These results helped to interpret our results for more complicated cases, serving as a benchmark for the case of complete randomness. We also analyzed two natural fracture networks. These results showed clear deviations from the ideal case, deviations useful in describing subtler aspects of order among fractures.

A key idea of this paper is the use of the anisotropic pair-correlation function $g(r, \theta)$ to analyze directional inner correlations between fractures and branches. It recommends to employ subsets of objects comprising fractures of similar azimuth. For each subset, some directions (θ_i, with $i = 1, 2, \ldots$) of interest are considered in order to study alignments of their object centers. One of the θ_i is (or slightly deviates from) the main azimuth of objects and reflects organization due to interactions between fractures of the same set during their growth. The Oman data set has shown that also other directions are of interest to study interactions and chronology between objects of two different sets.

In a nutshell, the proposed statistical method follows these five main steps:

1. Ensure the validity of the stationarity hypothesis.
2. Build marked points for both fractures and branches.
3. Study directionality: decide whether the pattern can be considered isotropic or determine main azimuthal directions and identify sets of objects.
4. If isotropy then use $g(r)$. Otherwise determine the $g(r, \theta_i)$ for the sets with θ_i the directions of main interest.
5. Discuss the form of $g(r)$ or of the $g(r, \theta_i)$. Pay attention for maxima, clustering, and repulsion.
6. Use the mark-correlation functions k_{mm} and $\gamma_m(r)$ (preferably for the fractures) to get information on the spatial correlations of fracture length.

This means that it is not recommended to repeat the full statistics of this paper for each other 2D fracture network. It may be even sufficient to consider only one or two directions θ_i of special interest.

Future applications of this exploratory statistics workflow to other surface exposure and different planar sections through fracture systems may improve the understanding and classification of fracture networks. Indeed, subtle differences between networks may be detected and measured if similar fractured patterns are compared.

Finally, the information obtained using these statistical methods paves the way toward better mathematical models for stochastic simulations of three-dimensional fracture networks, which are needed for studies of the physical properties of fractured rock. Such statistical measures can be directly used to construct models managing interactions between marked point objects. The goodness-of-fit of such models can be tested by planar sections using the presented characteristics.

Appendix A: The Miles–Lantuéjoul Estimator

The Miles–Lantuéjoul sampling method is a general estimation principle in spatial statistics, created by Miles (1974) and Lantuéjoul (1978). It is used to estimate quantities describing the size distribution of randomly distributed planar and spatial systems of objects whose structure is assumed to be stationary. The basic idea is "minus-sampling": objects can only be observed within a window W, and objects only partly within W are ignored. The observations must be carefully weighted to achieve an unbiased estimation, and this method cannot "magically" incorporate information from very large objects. (For comparison, "plus-sampling" assumes that all objects within W and hit by W can be measured completely.)

Here, we present the Miles–Lantuéjoul estimator in the case of segments in a plane. The aim is to estimate a histogram of segment lengths. We consider the bin $[l_k, l_{k+1}]$. The window is a rectangle with sides of lengths a and b and parallel to the x- and y-axes.

The total number of lower segment endpoints in W is denoted N. Only segments fully within W are measured, and their number denoted n. The segments are described as follows. Their reference points are their lower endpoints, and their segment lengths are denoted L_i for $i = 1, 2, \ldots, n$. The orientation of segment i is described by a rectangle with sides of lengths x_i and y_i that contains the segment as a diagonal, the sides being parallel to the x- and y-axes. In the case that segment i is parallel to the x-axis (or y-axis), $x_i = L_i$ and $y_i = 0$ (or $y_i = L_i$ and $x_i = 0$).

The estimator of the probability p_k that the segment length is in the bin $[l_k, l_{k+1}]$ is

$$p_k = \frac{ab}{N} \sum_{i=1}^{n} \frac{\delta_{ki}}{(a - x_i)(b - y_i)}, \tag{A1}$$

with

$$\delta_{ki} = 1 \text{ if } l_k \le L_i < l_{k+1} \text{ and } \delta_{ki} = 0 \text{ otherwise.} \tag{A2}$$

Appendix B: Estimating Pair-Correlation Functions and the Role of Bandwidths

This paper makes extensive use of statistics for pair-correlation functions (pcfs). This appendix explains some of the main ideas of the estimators we recommend. Note that estimators of $K(r)$, of the isotropic $g(r)$ and of the mark-correlation functions are available in the statistical software R, in its SpatStat package. They are explained in detail in Illian et al. (2008) and Baddeley et al. (2016). The following is written for readers who want to be informed in a simple and concise way to make their own implementation.

We start with some explanation about $g(r)$ considering a pattern of n marked points. The statistics are based on the intercenter distances $d(c_i, c_j)$, where c_i and c_j are the centers of two separated objects which lie in a rectangular window W of side-lengths a (along the x-axis) and b (along the y-axis). To obtain an estimate of $g(r)$, the center pairs of a distance close to r are collected. The value of r should be larger than the minimum intercenter distance.

We used a kernel estimator, in order to obtain smooth curves for empirical pcfs. The degree of smoothness is controlled by a so-called "bandwidth" parameter h. More precisely, we used the simplest (and best for our purpose) kernel: the "box kernel," where all center pairs with intercenter distance between $r - h$ and $r + h$ are included, ignoring the true distances. In other words, for a reference center c_i all centers in the ring centered at c_i of radius r and width $2h$ are considered with equal weight.

The bandwidth h strongly influences the results: at large h, the curves obtained are smooth and fine details are smoothed away, whereas at small h, the curves become spiky. Optimally choosing h is somewhat of an art: a simple method is to start with:

$$h = \frac{0.1}{\sqrt{P_{20}}}, \tag{B1}$$

then search for an appropriate value of h by experimentation. The aim is to obtain smooth curves that retain interesting details. Values of h used in this paper are either constant or adapted, that is, piece-wise constant and increasing with r. Table B1 presents all bandwidth values used in this paper.

Table B1
Bandwidths h (m) Used in the Figures

Figure	h_{iso}	h_{0°	h_{90°	h_{130°
4a	0.35	0.35	0.35	0.35
4b	0.15	0.4	0.4	0.4
5a	0.3	0.7	0.7	0.7
5b	0.2	0.35	0.35	0.35
6a, k_{mm}	0.35	0.35	0.35	0.35
6a, γ_{mm}	0.35	0.35	0.35	0.35
6b, k_{mm}	0.4	0.8	0.95	0.8
6b, γ_{mm}	0.45	0.9	0.9	0.9
	h_{iso}	h_{40°		h_{130°
9a	(1.8, 1.9, 16)	(1.8, 2.6, 16)		(1.9, 5, 8.8)
9b	(0.8, 1.0, 8)	(1, 2.9, 12.8)		(1.5, 1.8, 14.4)
10a	2	(4, 7, 12)		(2, 5, 14.4)
10b	1.5	(1.9, 4, 12)		(2, 2.7, 14.4)
11a	2	(1.9, 3.6, 22.4)		(2.6, 3.2, 14.4)
11b	(0.8, 1.4, 8)	(1.9, 3.5, 16.8)		(1.6, 2, 20)
12a, k_{mm}	(2.7, 3.6, 16)	(5, 6.5, 14.4)		(5, 6.5, 5.6)
12a, γ_{mm}	(5.5, 9.5, 6.4)	(7, 14.5, 7.2)		(5, 12, 8.0)
12b, k_{mm}	(1, 3, 8.0)	(4, 6, 19.2)		(5, 10, 12.8)
12b, γ_{mm}	(2, 4, 9.6)	(4.5, 6, 19.2)		(6, 10, 12.8)
	h_{iso}	h_{50°	h_{130°	h_{170°
15a	0.03	(0.035, 0.08, 0.33)	(0.03, 0.08, 0.33)	(0.07, 0.1, 0.33)
15b	0.027	(0.027, 0.05, 0.33)	(0.027, 0.05, 0.33)	(0.027, 0.05, 0.33)
	h_{iso}	h_{50°	h_{140°	h_{60°
16a, N50	0.06	(0.05, 0.085, 0.09)	0.06	(0.035, 0.089, 0.09)
16b, N50	0.02	(0.03, 0.045, 0.075)	0.04	(0.035, 0.05, 0.3)
	h_{iso}	h_{40°		h_{130°
16a, N130	0.07	(0.07, 0.11, 0.6)		(0.07, 0.11, 0.6)
16b, N130	0.03	(0.05, 0.1, 0.3)		(0.05, 0.1, 0.3)
	h_{iso}	h_{80°		h_{170°
16a, N170	0.07	(0.07, 0.15, 0.6)		(0.07, 0.15, 0.6)
16b, N170	0.04	(0.04, 0.1, 0.15)		(0.04, 0.1, 0.15)
	h_{iso}	h_{50°	h_{130°	h_{170°
17a, k_{mm}	(0.09, 0.2, 0.7)	(0.35, 0.55, 0.7)	(0.35, 0.55, 0.7)	(0.35, 0.55, 0.7)
17a, γ_{mm}	0.15	0.6	0.6	0.6
17b, k_{mm}	(0.027, 0.08, 0.4)	(0.1, 0.25, 0.4)	(0.1, 0.25, 0.4)	(0.1, 0.25, 0.4)
17b, γ_{mm}	0.075	(0.09, 0.2, 0.7)	(0.09, 0.2, 0.7)	(0.09, 0.2, 0.7)

Note. For adapted bandwidth, we use the notation ($h_{r\le t}$, $h_{r>t}$, t), where t is a threshold distance (m).

We now explain the estimator of $g(r)$ in two steps: first we explain a naive biased estimator $g_n(r)$ and then the recommended estimator $\hat{g}(r)$ with edge-correction. Such a correction is necessary since for a small window W many centers may miss their partners at large distances r.

The naive estimator $g_n(r)$ is the ratio $Nc(r)/N$ of two numbers of center pairs divided by corresponding areas. N is $\frac{n(n-1)}{2} \cdot \frac{1}{ab}$, the number of all center pairs in W divided by its area ab. $N_c(r)$ is the number of all center pairs with intercenter distance between $r-h$ and $r+h$, divided by the approximation $4\pi{\cdot}r{\cdot}h$ of the area of the ring of radius r and width $2h$. This yields

$$g_n(r) = N_c(r)/N = \frac{2 \cdot ab}{n(n-1)} \cdot \frac{N_c(r)}{4\pi \cdot r \cdot h} = \frac{2 \cdot (ab)^2}{n(n-1)} \cdot \frac{N_c(r)}{4\pi \cdot r \cdot h \cdot ab}. \tag{B2}$$

In order to understand the edge-corrected estimator $\hat{g}(r)$, we rewrite $N_c(r)/ab$ as a sum over all center pairs:

$$N_c(r) = \sum_{i=1}^{n} \sum_{j=i+1}^{n} \mathbb{1}\left(-h \le d\left(c_i, c_j\right) - r \le h\right) / ab, \tag{B3}$$

where $\mathbb{1}(\cdot) = 1$ if the inequalities are satisfied and =0 otherwise.

Then, the summands $\mathbb{1}(\cdot)/ab$ are modified by giving the rare cases of large inter-center distances more weight. The simple ab is replaced by $(a - a_{ij})(b - b_{ij})$, where a_{ij} is the absolute value of the x-component of $(c_i - c_j)$; similarly b_{ij} is the absolute value of the y-component of $(c_i - c_j)$. This yields the final form of $\hat{g}(r)$:

$$\hat{g}(r) = \frac{2 \cdot (ab)^2}{n(n-1)} \cdot \frac{1}{4\pi \cdot r \cdot h} \sum_{i=1}^{n} \sum_{j=i+1}^{n} \frac{\mathbb{1}\left(-h \le d\left(c_i, c_j\right) - r \le h\right)}{\left(a - a_{ij}\right)\left(b - b_{ij}\right)}. \tag{B4}$$

Finally, we focus on the anisotropic pcf $g(r, \theta)$. Additionally to the distance $d(c_i, c_j)$ between centers c_i and c_j the (smaller) angle between the line through c_i and c_j and the North, $\angle(c_i, c_j)$, plays a role. Again, the window is W, of size ab. The number of centers is again denoted by n. As for $\hat{g}(r)$, a distance r is considered and a bandwidth h plays a role, but now additionally a direction θ and a direction precision δ is employed. Only all center pairs with $-\delta \le \angle(c_i, c_j) - \theta \le \delta$ are considered; the corresponding arc is $\alpha = \frac{2\delta}{180}\pi$. We worked with $\delta = 5°$.

The estimator $\hat{g}(r, \theta)$ is a modification of $\hat{g}(r)$: the indicator $\mathbb{1}\left(-h \le d\left(c_i, c_j\right) - r \le h\right)$ is multiplied with the angle indicator $\mathbb{1}\left(-\delta \le \angle\left(c_i, c_j\right) - \theta \le \delta\right)$ and divided by α instead of 2π.

Appendix C: Short-Range and Long-Range Order

The terms "short-range order" and "long-range order" have origins in physics and chemistry, in the context of atomic patterns. Here, we use them in a slightly modified meaning, with the hope of making them useful for spatial statistics in geological applications.

The term "long-range order" is in full agreement with the classical definition when applied to a lattice of points. For a quadratic lattice with side length a, the pcf has poles at $r = a$, $r = \sqrt{2}a$, $r = 2a$, etc. When its points are somewhat randomly moved, the pcf would have maxima at these values of r.

In geological contexts and at scales suitable for fractures, such patterns are atypical. Indeed, a pcf with maxima at some r-values a and $\sqrt{2}a$ is somewhat remarkable. In such cases, we use the term "long-range order" to emphasize the repeatability of the pattern.

When a pcf has at least one clear maximum at some r-value, this marks a clear difference from a Poisson process (i.e., patterns of complete randomness with pcfs that do not have any maxima). To highlight that this is somewhat remarkable, we herein use the term "short-range order" to emphasize that there is a unique most frequent interpoint distance.

When describing short-range and long-range order, the r-values at the maxima are important because they indicate frequent interpoint distances. The heights of the maxima are also important because they characterize the relative frequencies of these distances.

Data Availability Statement

Data used in this study have been taken from the literature (see, e.g., Odling, 1997; Zeeb et al., 2013). We used SKUA-Gocad Software and Geode-Solutions (2022a, 2022b) to convert these data into a realization of marked points which are provided as supplementary data. A plugin of the OpenGeode platform named OpenGeode-PointProcess has been used for statistical analysis of marked point process. This software belongs to ASGA (Association Scientifique pour la Geology et ses Applications), therefore is not publicly available. ASGA manages the RING Consortium (www.ring-team.org/consortium) and provides access to the research material only to its members/sponsors. Tools and parameters are presented in detail in the paper (see Appendix) and most of the analysis can be done using SpatStat R package with the guidance of Baddeley et al. (2016).

Acknowledgments
This work was performed in the frame of the RING project (http://ring.geores-sources.univ-lorraine.fr/) at the Université de Lorraine. We acknowledge support from industrial and academic sponsors of the RING-GOCAD Consortium managed by ASGA. All data used in this paper have already been published in the literature. We thank Conny Zeeb and Noelle Odling for providing the data for the two natural fracture networks. We are grateful to Gautier Laurent and Guillaume Caumon for their constructive remarks and to reviewers David J. Sanderson and Tom Manzocchi. We also particularly thank editor Isabelle Manighetti for encouraging us to make the extensive revisions of the original manuscript. Finally, we are thankful to AspenTech for the SKUA-Gocad Software and development kit and to Geode-Solutions for the OpenGeode open source project Geode-Solutions (2022b) and proprietary software and API Geode-Solutions (2022a).

References

Agterberg, F. (2014). *Geomathematics: Theoretical foundations, applications and future developments*. Springer.
Baddeley, A., Rubak, E., & Turner, R. (2016). *Spatial point patterns: Methodology and applications with R* (OCLC: ocn933300812). CRC Press/Taylor & Francis Group.
Balberg, I., & Binenbaum, N. (1983). Computer study of the percolation threshold in a two-dimensional anisotropic system of conducting sticks. *Physical Review B*, *28*(7), 3799–3812. https://doi.org/10.1103/PhysRevB.28.3799
Barton, C., & Hsieh, P. (1989). Physical and hydrological-flow properties of fractures. In *Field trip guidebook T385* (p. 36). AGU.
Bergbauer, S., & Pollard, D. D. (2004). A new conceptual fold-fracture model including prefolding joints, based on the Emigrant Gap anticline, Wyoming. *The Geological Society of America Bulletin*, *116*(3), 294. https://doi.org/10.1130/B25225.1
Berkowitz, B. (1995). Analysis of fracture network connectivity using percolation theory. *Mathematical Geology*, *27*(4), 467–483. https://doi.org/10.1007/BF02084422
Bistacchi, A., Mittempergher, S., Martinelli, M., & Storti, F. (2020). On a new robust workflow for the statistical and spatial analysis of fracture data collected with scanlines (or the importance of stationarity). *Solid Earth*, *11*(6), 18. https://doi.org/10.5194/se-2020-83
Bonneau, F., Caumon, G., & Renard, P. (2016). Impact of a stochastic sequential initiation of fractures on the spatial correlations and connectivity of discrete fracture networks: Stochastic sequential DFN simulation. *Journal of Geophysical Research: Solid Earth*, *121*, 5641–5658. https://doi.org/10.1002/2015JB012451
Bonnet, E., Bour, O., Odling, N. E., Davy, P., Main, I., Cowie, P., & Berkowitz, B. (2001). Scaling of fracture systems in geological media. *Reviews of Geophysics*, *39*(3), 347–383. https://doi.org/10.1029/1999RG000074
Bour, O., Davy, P., Darcel, C., & Odling, N. (2002). A statistical scaling model for fracture network geometry, with validation on a multiscale mapping of a Joint network (Hornelen Basin, Norway). *Journal of Geophysical Research*, *107*(B6), 2113. https://doi.org/10.1029/2001JB000176
Cherpeau, N., & Caumon, G. (2015). Stochastic structural modelling in sparse data situations. *Petroleum Geoscience*, *21*(4), 233–247. https://doi.org/10.1144/petgeo2013-030
Cherpeau, N., Caumon, G., & Lévy, B. (2010). Stochastic simulation of fault networks from 2D seismic lines. In *SEG Technical Program expanded abstracts 2010* (pp. 2366–2370). Society of Exploration Geophysicists. https://doi.org/10.1190/1.3513325
Chiu, S. N., Stoyan, D., Kendall, W. S., & Mecke, J. (2013). *Stochastic geometry and its applications* (3rd ed.). John Wiley & Sons, Ltd. https://doi.org/10.1002/9781118658222
Darcel, C., Bour, O., & Davy, P. (2003a). Cross-correlation between length and position in real fracture networks. *Geophysical Research Letters*, *30*(12), 1650. https://doi.org/10.1029/2003GL017174
Darcel, C., Bour, O., & Davy, P. (2003b). Stereological analysis of Fractal fracture networks. *Journal of Geophysical Research*, *108*(B9), 2451. https://doi.org/10.1029/2002JB002091
Davy, P., Le Goc, R., Darcel, C., Bour, O., de Dreuzy, J. R., & Munier, R. (2010). A likely universal model of fracture scaling and its consequence for crustal hydromechanics. *Journal of Geophysical Research*, *115*, B10411. https://doi.org/10.1029/2009JB007043
de Joussineau, G., & Aydin, A. (2007). The evolution of the damage zone with fault growth in sandstone and its multiscale characteristics. *Journal of Geophysical Research*, *112*, B12401. https://doi.org/10.1029/2006JB004711
Dershowitz, W., & Einstein, H. H. (1988). Characterizing rock joint geometry with joint system models. *Rock Mechanics and Rock Engineering*, *21*(1), 21–51. https://doi.org/10.1007/BF01019674
Dershowitz, W., & Herda, H. H. (1992). Interpretation of fracture spacing and intensity. In *The 33th US Symposium on Rock Mechanics (USRMS)*. American Rock Mechanics Association.
Dershowitz, W., Mauldon, M., & La Pointe, P. (2020). Fracture abundance measures. In *54th US Rock Mechanics/Geomechanics Symposium*.
Geode-Solutions. (2022a). Geode-ExplicitModeling [software]. Zenodo. https://doi.org/10.5281/ZENODO.6592422
Geode-Solutions. (2022b). OpenGeode framework [software]. Zenodo. https://doi.org/10.5281/ZENODO.3610370
Gillespie, P. A., Howard, C. B., Walsh, J. J., & Watterson, J. (1993). Measurement and characterisation of spatial distributions of fractures. *Tectonophysics*, *226*(1), 113–141. https://doi.org/10.1016/0040-1951(93)90114-Y
Gillespie, P. A., Johnston, J. D., Loriga, M. A., McCaffrey, K. J. W., Walsh, J. J., & Watterson, J. (1999). Influence of layering on vein systematics in line samples. *Geological Society, London, Special Publications*, *155*(1), 35–56. https://doi.org/10.1144/GSL.SP.1999.155.01.05
Gomez-Rivas, E., Bons, P. D., Koehn, D., Urai, J. L., Arndt, M., Virgo, S., et al. (2014). The Jabal Akhdar dome in the Oman Mountains: Evolution of a dynamic fracture system. *American Journal of Science*, *314*(7), 1104–1139. https://doi.org/10.2475/07.2014.02
Hardebol, N. J., Maier, C., Nick, H., Geiger, S., Bertotti, G., & Boro, H. (2015). Multiscale fracture network characterization and impact on flow: A case study on the Latemar carbonate platform. *Journal of Geophysical Research: Solid Earth*, *120*, 8197–8222. https://doi.org/10.1002/2015JB011879
Hentschel, H., & Procaccia, I. (1983). The infinite number of generalized dimensions of fractals and strange attractors. *Physica D: Nonlinear Phenomena*, *8*(3), 435–444. https://doi.org/10.1016/0167-2789(83)90235-X
Hilgers, C., Kirschner, D. L., Breton, J.-P., & Urai, J. L. (2006). Fracture sealing and fluid overpressures in limestones of the Jabal Akhdar dome, Oman Mountains. *Geofluids*, *6*(2), 168–184. https://doi.org/10.1111/j.1468-8123.2006.00141.x
Holland, M., Saxena, N., & Urai, J. L. (2009). Evolution of fractures in a highly dynamic thermal, hydraulic, and mechanical system—(II) Remote sensing fracture analysis, Jabal Shams, Oman Mountains. *GeoArabia*, *14*(3), 163–194. https://doi.org/10.2113/geoarabia1403163

Holland, M., Urai, J. L., Muchez, P., & Willemse, E. J. (2009). Evolution of fractures in a highly dynamic thermal, hydraulic, and mechanical system - (I) Field observations in Mesozoic Carbonates, Jabal Shams, Oman Mountains. *GeoArabia*, *14*(1), 57–110. https://doi.org/10.2113/geoarabia140157

Illian, J., Penttinen, A., Stoyan, H., & Stoyan, D. (2008). *Statistical analysis and modelling of spatial point patterns*. John Wiley & Sons, Ltd. https://doi.org/10.1002/9780470725160

Ivanova, V. M., Sousa, R., Murrihy, B., & Einstein, H. H. (2014). Mathematical algorithm development and parametric studies with the GEOFRAC three-dimensional stochastic model of natural rock fracture systems. *Computers & Geosciences*, *67*, 100–109. https://doi.org/10.1016/j.cageo.2013.12.004

Ji, S., Zhu, Z., & Wang, Z. (1998). Relationship between joint spacing and bed thickness in sedimentary rocks: Effects of interbed slip. *Geological Magazine*, *135*(5), 637–655. https://doi.org/10.1017/S0016756898001459

Josnin, J.-Y., Jourde, H., Fénart, P., & Bidaux, P. (2002). A three-dimensional model to simulate joint networks in layered rocks. *Canadian Journal of Earth Sciences*, *39*(10), 1443–1455. Retrieved from http://www.nrcresearchpress.com/doi/abs/10.1139/e02-043

Kim, Y.-S., Peacock, D. C., & Sanderson, D. J. (2004). Fault damage zones. *Journal of Structural Geology*, *26*(3), 503–517. https://doi.org/10.1016/j.jsg.2003.08.002

Koike, K., Kubo, T., Liu, C., Masoud, A., Amano, K., Kurihara, A., et al. (2015). 3D geostatistical modeling of fracture system in a granitic massif to characterize hydraulic properties and fracture distribution. *Tectonophysics*, *660*, 1–16. https://doi.org/10.1016/j.tecto.2015.06.008

Konietzky, H., Li, X., & Chen, W. (2020). Lifetime prediction of rocks. In B. Shen, O. Stephansson, & M. Rinne (Eds.), *Modelling rock fracturing processes* (pp. 475–529). Springer International Publishing. https://doi.org/10.1007/978-3-030-35525-8_19

Lantuéjoul, C. (1978). Computation of the histograms of the number of edges and neighbours of cells in a tessellation. In R. Miles & J. Serra (Eds.), *Geometrical probability and biological structures: Buffon's 200th anniversary* (Vol. 23, pp. 323–329). Springer.

Laubach, S. E., Lander, R. H., Criscenti, L. J., Anovitz, L. M., Urai, J. L., Pollyea, R. M., et al. (2019). The role of chemistry in fracture pattern development and opportunities to advance interpretations of geological materials. *Reviews of Geophysics*, *57*, 1065–1111. https://doi.org/10.1029/2019RG000671

Lei, Q., Latham, J.-P., & Tsang, C.-F. (2017). The use of discrete fracture networks for modelling coupled geomechanical and hydrological behaviour of fractured rocks. *Computers and Geotechnics*, *85*, 151–176. https://doi.org/10.1016/j.compgeo.2016.12.024

Macé, L., Souche, L., & Mallet, J.-L. (2004). 3D Fracture characterization based on geomechanics and geologic data uncertainties. In *ECMOR IX—9th European Conference on the Mathematics of Oil Recovery*. European Association of Geoscientists & Engineers. https://doi.org/10.3997/2214-4609-pdb.9.A025

Manzocchi, T. (2002). The connectivity of two-dimensional networks of spatially correlated fractures. *Water Resources Research*, *38*(9), 1162. https://doi.org/10.1029/2000WR000180

Manzocchi, T., Walsh, J., & Bailey, W. (2009). Population scaling biases in map samples of power-law fault systems. *Journal of Structural Geology*, *31*(12), 1612–1626. https://doi.org/10.1016/j.jsg.2009.06.004

Martinelli, M., Bistacchi, A., Mittempergher, S., Bonneau, F., Balsamo, F., Caumon, G., & Meda, M. (2020). Damage zone characterization combining scan-line and scan-area analysis on a km-scale Digital Outcrop Model: The Qala Fault (Gozo). *Journal of Structural Geology*, *140*, 104144. https://doi.org/10.1016/j.jsg.2020.104144

Miles, R. (1974). On the elimination of edge effects in planar sampling. In R. Davidson, D. G. Kendall, & E. F. Harding (Eds.), *Stochastic geometry: A tribute to the memory of Rollo Davidson* (Vol. 10, pp. 228–247). Wiley.

Odling, N. E. (1997). Scaling and connectivity of joint systems in sandstones from western Norway. *Journal of Structural Geology*, *19*(10), 1257–1271. https://doi.org/10.1016/S0191-8141(97)00041-2

Odling, N. E., Gillespie, P., Bourgine, B., Castaing, C., Chiles, J. P., Christensen, N. P., et al. (1999). Variations in fracture system geometry and their implications for fluid flow in fractures hydrocarbon reservoirs. *Petroleum Geoscience*, *5*(4), 373–384. https://doi.org/10.1144/petgeo.5.4.373

Peacock, D., & Sanderson, D. (2018). Structural analyses and fracture network characterisation: Seven pillars of wisdom. *Earth-Science Reviews*, *184*, 13–28. https://doi.org/10.1016/j.earscirev.2018.06.006

Pollard, D. D., & Aydin, A. (1988). Progress in understanding jointing over the past century. *GSA Bulletin*, *100*(8), 1181–1204. https://doi.org/10.1130/0016-7606(1988)100<1181:PIUJOT>2.3.CO;2

Pyrcz, M., & Deutsch, C. V. (2014). *Geostatistical reservoir modeling* (2nd ed.). Oxford University Press.

Renard, P., & Allard, D. (2013). Connectivity metrics for subsurface flow and transport. *Advances in Water Resources*, *51*, 168–196. https://doi.org/10.1016/j.advwatres.2011.12.001

Saevik, P. N., & Nixon, C. W. (2017). Inclusion of topological measurements into analytic estimates of effective permeability in fractured media: Fracture permeability from topology. *Water Resources Research*, *53*, 9424–9443. https://doi.org/10.1002/2017WR020943

Sanderson, D. J., & Nixon, C. W. (2015). The use of topology in fracture network characterization. *Journal of Structural Geology*, *72*, 55–66. https://doi.org/10.1016/j.jsg.2015.01.005

Sanderson, D. J., & Nixon, C. W. (2018). Topology, connectivity and percolation in fracture networks. *Journal of Structural Geology*, *115*, 167–177. https://doi.org/10.1016/j.jsg.2018.07.011

Sanderson, D. J., & Peacock, D. C. (2019). Line sampling of fracture swarms and corridors. *Journal of Structural Geology*, *122*, 27–37. https://doi.org/10.1016/j.jsg.2019.02.006

Sanderson, D. J., Peacock, D. C., Nixon, C. W., & Rotevatn, A. (2019). Graph theory and the analysis of fracture networks. *Journal of Structural Geology*, *125*, 155–165. https://doi.org/10.1016/j.jsg.2018.04.011

Schwartz, D. P., & Sibson, R. (1989). Proceedings of conference XLV; a workshop on fault segmentation and controls of rupture initiation and termination (Report No. 89-315). Retrieved from http://pubs.er.usgs.gov/publication/ofr89315

Scott, C. P., Giampietro, T., Brigham, C., Leclerc, F., Manighetti, I., Arrowsmith, J. R., & Mattéo, L. (2022). Semiautomatic algorithm to map tectonic faults and measure scarp height from topography applied to the volcanic tablelands and the hurricane fault, western US. *Lithosphere*, *2021*(Special 2), 9031662. https://doi.org/10.2113/2021/9031662

Segall, P., & Pollard, D. (1980). Mechanics of discontinuous faults. *Journal of Geophysical Research*, *85*(B8), 4337–4350. https://doi.org/10.1029/JB085iB08p04337

Shakiba, M., Lake, L. W., Gale, J. F., & Pyrcz, M. J. (2022). Multiscale spatial analysis of fracture arrangement and pattern reconstruction using Ripley's K-function. *Journal of Structural Geology*, *155*, 104531. https://doi.org/10.1016/j.jsg.2022.104531

Stoyan, D. (1994). Caution with "fractal" point patterns!. *Statistics*, *25*(3), 267–270. https://doi.org/10.1080/02331889408802450

Stoyan, D. (2021). Stochastic geometry in the geosciences. In B. Daya Sagar, Q. Cheng, J. McKinley, & F. Agterberg (Eds.), *Encyclopedia of mathematical geosciences* (pp. 1–10). Springer International Publishing.

Stoyan, D., & Stoyan, H. (1994). *Fractals, random shapes, and point fields: Methods of geometrical statistics*. Wiley.

Sui, L., Yu, J., Cang, D., Miao, W., Wang, H., Zhang, J., et al. (2019). The fractal description model of rock fracture networks characterization. *Chaos, Solitons & Fractals*, *129*, 71–76. https://doi.org/10.1016/j.chaos.2019.07.055

Wu, H., & Pollard, D. D. (1995). An experimental study of the relationship between joint spacing and layer thickness. *Journal of Structural Geology*, *17*(6), 887–905. https://doi.org/10.1016/0191-8141(94)00099-L

Zeeb, C., Gomez-Rivas, E., Bons, P. D., & Blum, P. (2013). Evaluation of sampling methods for fracture network characterization using outcrops. *AAPG Bulletin*, *97*(9), 1545–1566. https://doi.org/10.1306/02131312042